The MAP4K4-STRIPAK complex promotes growth and tissue invasion in medulloblastoma

Jessica Migliavacca[1], Buket Züllig[1], Charles Capdeville[1], Michael Grotzer[2] and Martin Baumgartner[1,*]

[1] Division of Oncology, Children's Research Center, University Children's Hospital Zürich, Zürich, Switzerland

[2] Division of Oncology, University Children's Hospital Zürich, Zürich, Switzerland

*e-mail: Martin.Baumgartner@kispi.uzh.ch

Abstract

Proliferation and motility are mutually exclusive biological processes associated with cancer that depend on precise control of upstream signaling pathways with overlapping functionalities. We find that STRN3 and STRN4 scaffold subunits of the STRIPAK complex interact with MAP4K4 for pathway regulation in medulloblastoma. Disruption of the MAP4K4-STRIPAK complex impairs growth factor-induced migration and tissue invasion and stalls YAP/TAZ target gene expression and oncogenic growth. The migration promoting functions of the MAP4K4-STRIPAK complex involve the activation of novel PKCs and the phosphorylation of the membrane targeting S157 residue of VASP through MAP4K4. The anti-proliferative effect of complex disruption is associated with reduced YAP/TAZ target gene expression and results in repressed tumor growth in the brain tissue. This dichotomous functionality of the STRIPAK complex in migration and proliferation control acts through MAP4K4 regulation in tumor cells and provides relevant mechanistic insights into novel tumorigenic functions of the STRIPAK complex in medulloblastoma.

Introduction

Medulloblastoma (MB) is the most common malignant brain tumor in children[1]. Four distinct molecular subgroups (Wingless (WNT), Sonic Hedgehog (SHH), group 3, and group 4) can be discriminated with a total of 12 subtypes that display differences in genetic alterations, clinical features, and outcomes[2–4]. With multimodal therapies, the survival rates across all MB age groups have reached 70-85%[5–7]. However, the characteristic tendency of MB cells to locally infiltrate the cerebrospinal fluid (CSF) via leptomeningeal dissemination reduces the efficacy of current treatments[8]. One key driver of tissue invasion and growth in MB is the Fibroblast Growth Factor Receptor (FGFR) signaling pathway[9,10] The molecular mechanisms underlying MB tissue infiltration and growth are poorly understood and cannot be specifically targeted[11]. Infiltration, dissemination, and long-distance spreading of tumor cells are mediated by the transient or permanent induction of cell motility[12]. Cell migration relies on the complex orchestration of cytoskeletal remodeling, membrane dynamics, and cell adhesion to the extracellular matrix (ECM)[13–15]. Parallel, potentially redundant signaling pathways control these processes, and anti-dissemination therapies should specifically target the pro-migratory activity of a central component that integrates signals of several pathways.

We have identified the serine/threonine mitogen-activated protein kinase kinase kinase kinase 4 (MAP4K4/HGK/NIK), which is upregulated in MB patient samples, as a critical promoter of receptor tyrosine kinase (RTK)-induced MB cell dissemination[16,17]. MAP4K4 was originally identified as a Ste20 germinal center-like kinase[18] involved in the activation of the c-jun N-terminal kinase (JNK)[19,20]. MAP4K4 controls a wide range of biological processes[21–26], which can be explained by the interaction of MAP4K4 with a range of structurally and functionally different effectors. The pro-migratory function of MAP4K4 is in part due to its capability to directly phosphorylate the ezrin, radixin, moesin (ERM) proteins, which mediate lamellipodium formation in response to growth-factor (GF) stimulation[27]. MAP4K4 directly couples GF signaling to actin polymerization through phosphorylation of the actin-related protein 2 (Arp2) subunit of the Arp2/3 complex, which increases its actin nucleation activity and triggers membrane protrusion in response to EGF[28]. In MB, MAP4K4 promotes turnover and activation of the receptor tyrosine kinase c-MET and of the β-1 integrin adhesion receptor, which is necessary for membrane protrusion at the leading edge of invading cells[17]. However, the mechanisms orchestrating and balancing oncogenic functions of MAP4K4 in MB and other solid tumors remain unknown.

53 Using proximity-dependent biotin identification (BioID), we identified MAP4K4 as a component of the
54 recently identified Striatin-interacting phosphatase and kinase (STRIPAK) complex[29–31] in MB cells. We
55 explored whether MAP4K4-STRIPAK components are implicated in FGFR-driven cell dissemination,
56 tissue invasion and growth in MB, and we identified underlying changes in relevant signaling pathways
57 by kinase activity profiling. Our study identified the MAP4K4-STRIPAK complex as a central hub and
58 bifurcation point, which orchestrates tissue invasion and growth in MB tumors. It provides relevant
59 mechanistic insights in the regulation of these central processes in MB, which will contribute to the
60 design of more effective therapies for this devastating disease in the future.

61 **Results**

62 *MAP4K4 is a component of the STRIPAK complex in MB cells*

63 We used BioID to assess the MAP4K4 interactome and identified proteins biotinylated by FLAG-
64 tagged N- or C-terminally biotin ligase-fused (BioID2[32]) full-length MAP4K4 (BioID2-MAP4K4 and
65 MAP4K4-BioID2) or BioID2-FLAG alone through mass spectrometry (MS)[33,34] (Figure S1a). The
66 expression of 3xFLAG-tagged MAP4K4-BioID2 was confirmed by anti-FLAG immunoblot (IB) analysis
67 and of biotinylation activity by horseradish peroxidase (HRP)-coupled streptavidin binding (Figure 1a).
68 Biotinylated proteins were enriched by affinity-capturing using streptavidin-conjugated beads and
69 subjected to MS. We identified a total of 156 MAP4K4-specific proteins (Figure 1b, Table S1). Gene
70 ontology (GO) analysis with these proteins predicted functions such as endosomal transport[17], actin
71 polymerization[28], or regulation of cell adhesion[26] (Figure 1c), and found enrichment of components of
72 the STRIPAK complex (Figure 1c,d), a supramolecular scaffold held together by the striatin family
73 proteins (STRN, STRN3, STRN4). STRNs act as a regulatory subunit of the protein phosphatase PP2A
74 and are associated with STRN-interacting proteins (STRIP1/2) and with members of the germinal center
75 kinase (GCK) families (Figure 1e)[29,35]. We confirmed the interaction of 3xFLAG-BioID2-MAP4K4 with
76 STRN3, STRN4, and STRIP1 in HEK-293T cells (Figure 1f). In agreement with other studies[36–39], these
77 data confirm MAP4K4 association with the STRIPAK complex in cells, possibly through direct interaction
78 with STRN4 and STRN3.

79 We generated MB cell lines stably expressing either the 3XFLAG-BioID2-MAP4K4 fusion proteins or
80 BioID2 alone to test MAP4K4-STRIPAK complex interaction in these cells (Figure 1g). BioID2-MAP4K4
81 localized to the cytoplasm, the primary residency of MAP4K4, where it co-localized with biotinylated

82 proteins (Figure S1b). In contrast, BioID2 distributes throughout the cells, with enrichment in the nucleus.
83 Streptavidin affinity purification-MS and anti-FLAG immunoprecipitation confirmed the association of
84 MAP4K4 with the STRIPAK complex in MB cells (Figure 1h,i, Figure S1c, Table S2). Unlike other
85 germinal center kinases that have been reported to interact with STRIP1 in an activity-dependent
86 manner[40], inhibition of MAP4K4 by GNE-495 did not impact its constitutive association with STRN4,
87 STRN3, and STRIP1 (Figure S1d). We generated DAOY cells stably expressing 3XFLAG-tagged single
88 domains or truncated versions of MAP4K4 (Figure 1J). We found that N-terminally truncated MAP4K4
89 (ID1-ID2-CNH, 290-1273) pulled-down STRN4 and STRIP1 more effectively than C-terminally truncated
90 KD-ID1-ID2 (1-954) (Figure 1j,k). The kinase domain (KD, 1-289) or the intermediate domains (ID1, 290-
91 634 or ID2, 635-954) alone are not sufficient for pulling down STRN4 or STRIP1. Combined, these
92 results suggest that the citron homology domain (CNH, 954-1273) is required for MAP4K4-STRIPAK
93 interaction.

94 *STRIPAK complex is required for bFGF-induced collagen I invasion of MB cells*

95 STRIPAK complex members STRN4, STRN3, and STRIP1 are highly expressed in MB, and the
96 expression of STRNs correlates positively with site-specific phosphorylation of MAP4K4 in ID1 and
97 negatively with phosphorylation in ID2 *in vivo* ([41] and Figure S2a-d), suggesting a potential contribution
98 of these proteins to MAP4K4 regulation and MB pathogenesis. MAP4K4 promotes GF-induced MB cell
99 motility [16,17]. Hence, we first tested the implication of STRIPAK complex proteins in invasive motility in
100 DAOY (SHH) MB cell lines with a stable knockout (KO) of STRN4, STRN3, or STRIP1 (Figure S3a,b).
101 Using the spheroid collagen I invasion assay (SIA[42]), we observed that STRN4 KO abrogated GF-
102 induced cell invasion in DAOY cells, while KO of either STRIP1 or STRN3 had little or no effect (Figure
103 2A, Figure S3c).

104 We next determined the effect of simultaneous depletion of various STRIPAK components on GF-
105 induced migration using siRNA (Figure S3d,e). siSTRN4 confirmed STRN4 implication in bFGF-induced
106 collagen I invasion (Figure 2b). siSTRN3 also moderately reduced bFGF-induced invasion, whereas
107 siSTRIP1 caused a marked increase in both EGF- and bFGF-induced invasion (Figure 2b). siSTRIP1-
108 induced invasion was reverted when STRN4 was depleted simultaneously, indicating that the activity
109 repressed by STRIP1 involves a STRN3/4-dependent mechanism. Consistent with a functional
110 redundancy of STRN3 and STRN4, we observed that combined depletion of STRN3 and STRN4 had
111 an additive effect on EGF- or bFGF-induced collagen I invasion. Thus, STRN3 and STRN4 are, together

112 with MAP4K4, required for GF-induced collagen I invasion in MB, while STRIP1 has an inhibitory
113 function in this process.

114 STRIPAK complex can regulate associated kinases by enabling dephosphorylation through the
115 PP2A catalytic subunit[43,44]. Inhibition of PP2A sensitizes tumors to radiation and/or chemotherapy and
116 attenuates cell migration[45,46]. The PP2A inhibitor LB-100 decreased EGF- and bFGF-induced collagen
117 I invasion in a dose-dependent manner (Figure 2c, Figure S3f), without affecting cell viability (Figure
118 S3g). PP2A is thus not acting as a negative regulator of STRIPAK complex-associated MAP4K4 towards
119 GF-induced migration in MB, whereas STRN3/4 enable or facilitate the pro-invasive phenotype in GF-
120 stimulated MB cells.

121 *STRN3 controls GF-induced tissue expansion of tumor cell*

122 We used an *ex vivo* organotypic cerebellum slice culture model (OCSCs) to test STRIPAK implication
123 in MB tissue invasion. OCSCs maintain key features of the normal cerebellum cytoarchitecture and
124 constitute a physiologically relevant microenvironment model[47], where FGFR signaling contributes to
125 MB growth and tissue invasion[9]. We first tested whether the depletion of MAP4K4 or STRIPAK
126 components prevented growth and tissue invasion of DAOY cells (Figure 3a). Treatment of the co-
127 culture with EGF further enhances brain tissue invasion of the tumor cells. Depletion of MAP4K4 caused
128 rounded cell morphology and moderately reduced EGF-induced invasion (Figure 3b,c, Figure S4).
129 Depletion of STRN3 caused compaction of the tumor cell spheroids and prevented tissue invasion in
130 basal and EGF-stimulated conditions. Conversely, depletion of STRIP1 induced a more infiltrative
131 behavior, similar to what was observed *in vitro* (Figure 2b). The combined depletion of MAP4K4 and
132 STRN3 in DAOY cells caused a dramatic reduction of tumor area, which is not solely caused by reduced
133 cell proliferation (Figure 3c,d).

134 To confirm STRIPAK complex implication in tissue invasion, we implanted HD-MBO3 group 3 MB
135 cell lines KO for either MAP4K4, STRN4, STRN3, or STRIP1 (Figure S3b) in OCSCs. HD-MBO3 cells
136 are invasive and display a high growth rate[47]. We observed a moderate for MAP4K4 KO and a significant
137 reduction in the expansion for STRN3 KO cell-derived tumors, both after five days in basal or GF-
138 stimulated conditions (Figure 4a,b, Figure S5). Moreover, the number of EdU-positive nuclei was
139 considerably reduced in sgSTRN3 and sgSTRN4 but not in sgMAP4K4 cells (Figure 4c).

140 This data supports a model of STRIPAK-MAP4K4 complex control of growth and invasion of MB
141 tumor cells in the cerebellum tissue environment.

142 *Opposing functions of STRN3/4 and MAP4K4 in cell proliferation and YAP/TAZ target gene regulation*

143 STRN3 and STRN4 but not MAP4K4 depletion reduce MB cell growth in the cerebellum tissue. We
144 therefore tested MAP4K4-STRIPAK complex implication in colony-forming capability and clonal growth.
145 Depletion of MAP4K4 caused a marked increase in colony number independent of growth factor
146 stimulation in DAOY cells (Figure 5a). Conversely, depletion of STRN3 impaired colony formation and
147 clonal growth. Consistently depletion of either STRN4 or STRN3 caused a significant decrease in the
148 number of HD-MB03 colonies (Figure 5b), demonstrating that an intact STRIPAK complex is necessary
149 for clonal growth and colony expansion in MB cells. The effect of STRN3 depletion is particularly striking
150 under bFGF stimulation in HD-MB03, which promotes massive colony-forming activity in this group 3
151 MB model.

152 MAP4K4 is an activator of the Hippo tumor suppressor pathway, repressing YAP/TAZ target gene
153 expression and growth[48,49]. By antagonizing these growth-repressive MAP4K4 functions, the STRIPAK
154 complex halts Hippo pathway activation and promotes YAP/TAZ transcriptional activity[37,38,50,51]. We
155 found that MAP4K4 depletion significantly increased the expression of the YAP/TAZ target genes CTGF,
156 CYR61, and ANKRD1, which supports a Hippo-pathway activating function of MAP4K4 in MB cells
157 (Figure 5c,d). Conversely, suppression of STRN3 or STRN4 decreased transcription of these genes and
158 reverted the transcriptional activation induced by MAP4K4 depletion (Figure 5c).

159 Thus, MAP4K4 blocks MB cell proliferation, possibly by promoting the activation of the Hippo
160 pathway, whereas the STRIPAK complex and, in particular, STRN3, antagonizes Hippo activation and
161 is necessary for proliferation of MB cells (Figure S6).

162 *Novel protein kinases C are downstream effectors of MAP4K4 and STRN3 in promigratory signaling*

163 To identify effectors of the MAP4K4-STRIPAK complex downstream of FGFR activation, we profiled
164 changes in global kinase activities using the PamGene array technology. FGFR signaling caused
165 significantly increased activities of CDKs, PKC, SRC kinases, and FAK (Fig. 6a and Figure S7a). Several
166 of these and additional bFGF-induced kinase activities require the expression of MAP4K4 or STRIPAK
167 complex components (Figure 6a, Figure S7a). The most differently regulated Ser/Thr (STK) kinases
168 cluster in the AGC (cAMP-dependent, cGMP-dependent, and PKC) family of kinases (Figure S7b-e).
169 The activities of several AGC kinases were reduced when MAP4K4, STRN4, or STRN3 were
170 downregulated and increased in STRIP1-depleted cells. Consistently, depletion of MAP4K4, STRN3 or
171 STRN4, but not of STRIP1, caused a striking decrease in bFGF-induced activity of “novel” protein

172 kinases C (nPKCs, PKCδ, ε, η and θ) (Figure 6a). This suggests that MAP4K4 and STRIPAK
173 components are necessary for bFGF-induced activation of nPKCs and implies an effector role of nPKCs
174 downstream of MAP4K4 and STRN3. STRIP1 depletion increased the activity of a MAP4K4 signature
175 (Figure 6a), indicating that STRIP1 represses MAP4K4 in MB cells. The activated nPKC could constitute
176 druggable effector kinases to repress MB cell dissemination. We tested this possibility using inhibitors
177 specific for PKCδ (Rottlerin,[52]) and PKCθ (PKCθ I,[53]), and we observed a dose-dependent reduction of
178 bFGF-induced cell dissemination in DAOY cells (Figure 6b,c). The combination of both inhibitors further
179 reduced dissemination, suggesting that PKCδ and PKCθ functions in migration control are partially
180 overlapping (Figure 6d). Notably, the inhibition of classical PKCα, β, γ kinases by Bisindolylmaleimide I
181 (BIM) did not significantly repress MB cell dissemination (Figure 6e).
182 Collectively these data demonstrate that MAP4K4 and STRN3 promote a pro-migratory phenotype
183 in MB cells through the activation of common downstream effectors, which include novel but not classical
184 PKC family members.

185 *MAP4K4 and STRN3 enable bFGF-induced VASP Ser157 phosphorylation*

186 Depletion of MAP4K4 in bFGF-stimulated DAOY cells resulted in an overall decrease in the
187 phosphorylation of multiple STK and PTK consensus phosphorylation sites (Figure 7a, Figure S8, Table
188 S3). Many of these alterations were phenocopied by the depletion of STRN3 (Figure 7a). Conversely,
189 depletion of STRIP1 caused a global increase in the phosphorylation of STK substrates (Figure 7a,
190 Figure S8a). Phosphorylation profiles of PTK substrates were similar under all conditions (Figure 7a,
191 Figure S8b), with 23 substrates uniquely altered by MAP4K4 or STRN3 depletion (Figure 7b), including
192 the phospholipase C-γ (PLC-γ)-binding site[54] of FGFR1 ($FGFR_{Y766}$), and the SRC phosphorylation site
193 of AKT (AKT_{Y326})[55] (Figure 7c). Additionally, we observed the reduction of $FAK1_{Y570/576}$ and $FAK2_{Y573/579}$
194 phosphorylation in siMAP4K4 and siSTRN3, supporting the previously described role of MAP4K4 in
195 mediating FAK protein activation and focal adhesion assembly[17] (Figure 7c).
196 Exploring potential direct substrates of MAP4K4, we found that both MAP4K4 and STRN3 depletion
197 decreased the phosphorylation of $VASP_{S157}$ (Figure 7c), an F-actin elongation promoting factor[56,57].
198 Phosphorylation of S157 enables VASP translocation to the plasma membrane at the leading edge of
199 migrating cells[58,59] and regulates anti-capping activity[57]. In bFGF-stimulated cells, VASP accumulated
200 in the cortical cytoskeleton and the plasma membrane (Figure 7d), and in cells invading the brain tissue,
201 we observed filopodia only in control but not in MAP4K4 or STRN3-depleted cells (Figure 7e).

202 Consistently, depletion of MAP4K4 or STRN3 caused a robust reduction of bFGF-induced $VASP_{S157}$
203 phosphorylation in cells seeded on collagen I matrix (Figure 7f). Under the same condition, $VASP_{S157}$
204 phosphorylation is repressed by the MAP4K4 inhibitor GNE-595 in DAOY (Figure 7g) and HD-MBO3
205 cells (Figure 7h), supporting the notion that MAP4K4 directly phosphorylates this residue both under
206 basal condition as well as in response to FGFR activation.

207 Taken together, these results identified $VASP_{S157}$ phosphorylation as a novel effector mechanism of
208 MAP4K4 and STRN3 downstream of FGFR signaling (Figure 7i).

209 Discussion

210 We found that MAP4K4 interacts with the STRIPAK complex in MB cells and revealed a dual function
211 of the complex in growth and invasion control. An intact complex is necessary to maintain proliferation
212 and to drive migration and invasion induced by FGFR signaling. Depletion of MAP4K4 shifts complex
213 function towards increased clonal growth, increased YAP/TAZ target gene expression, increased tumor
214 cell proliferation in the cerebellar tissue, and decreased invasiveness. Depletion of STRN3 repressed
215 clonal growth, reduced YAP/TAZ target gene expression, and caused a significant reduction of tumor
216 growth and invasion in the cerebellar tissue. We furthermore discovered a novel function of the
217 MAP4K4-STRIPAK complex as a regulator of a set of migration and motility-associated effectors. These
218 include novel PKCs, FAK, and VASP, which mechanistically link complex functions to cytoskeleton
219 dynamics and cell motility. Thus, the MAP4K4-STRIPAK complex orchestrates signal transmission from
220 activated RTKs either towards an invasion or a growth-promoting phenotype in MB.

221 The interaction of the STRIPAK complex with MAP4K4 we found in MB confirms previous findings
222 describing direct interaction of STRIPAK with MST1/2, MST3/4, and MAP4Ks in other cell
223 models[35,39,43,44]. In MB, MAP4K4 represses YAP/TAZ target gene induction and its depletion promotes
224 colony formation and clonal growth, consistent with a canonical function of the STRIPAK complex[37,38,51],
225 where STRN3/4 block growth suppressing activities of MAP4K4 and additional kinases [48,49,60]. From
226 these findings, we conclude that MAP4K4 and STRN3 have opposing functions towards Hippo signaling
227 in MB and that the STRIPAK complex exerts a growth promoting function by suppressing the activity of
228 MAP4K4 specific to this context.

229 Parallel to antagonistic proliferation regulation of MAP4K4 and STRN3/4, we discovered that
230 MAP4K4 and STRN3/4 display a co-operative function towards bFGF-induced invasion control. We

231 identified AGC kinases and, in particular, novel PKCs (nPKCs), which are known promoters of
232 tumorigenesis[61], as downstream effectors of MAP4K-STRIPAK in invasion control, complementing
233 previous reports of tumor invasion control by STRIPAK with mechanistic insight[62,63]. nPKC-driven
234 invasion in MB may additionally involve the activation of adhesion and cytoskeleton-associated proteins
235 like ezrin- radixin-moesin (ERM), β1D integrin, and focal adhesion kinase (FAK)[64–68], the activity of latter
236 we also found increased by bFGF in a MAP4K4 and STRN3/4-dependent manner.

237 Inhibition of PKCδ and PKCθ but not of classical PKCs caused robust blockade of FGFR-driven
238 invasiveness. However, additional mechanisms of MAP4K-STRIPAK invasion regulation are likely. We
239 consider the phosphorylation of $VASP_{S157}$ particularly relevant because it couples STRIPAK function to
240 VASP localization, cytoskeleton regulation, and cell migration[57,58]. We propose that MAP4K4-mediated
241 $VASP_{Ser157}$ phosphorylation contributes to GF-induced MB cell motility and invasion by promoting
242 filopodia formation. In support of this is our observation in previous studies[9] and herein that tissue-
243 invading MB tumor cells display bFGF-induced, filopodia-like protrusions and that loss of these filopodia-
244 like protrusions is associated with reduced invasion. We found that MAP4K4 and STRN3 promote the
245 activity of several AGC kinases that are implicated in $VASP_{Ser157}$ phosphorylation, like PKG and PKD1[69].
246 VASP contributes to the etiology of prostate cancer, and $VASP_{Ser157}$ phosphorylation was recognized as
247 a marker of metastatic progression[70]. $VASP_{Ser157}$ phosphorylation by STRIPAK-controlled MAP4K4
248 could have broad implications in controlling invasion and viability of MB cells in the brain tissue by
249 providing signaling inputs from environment-sensing filopodia[71,72]. Growth cone turning and neuronal
250 pathfinding depend on filopodia function[73], whereby in particular low and high amplitude Ca^{2+} signaling
251 is involved in environment sensing and filopodia signaling[71]. Consistent with MB cells possibly exploiting
252 this feature of the developing nervous system, we detected a calcium-dependent kinase signature
253 downstream of bFGF-induced MAP4K4-STRIPAK. Depletion of STRIP1 increased GF-induced
254 migration in MB, perhaps by antagonizing MAP4K4 function. In support of this is an increase in MAP4K4
255 kinase activity signature after STRIP1 depletion, thus positioning STRIP1 as a negative regulator of
256 MAP4K4-driven mesenchymal invasiveness in MB. We observed a rounded, filopodia-depleted
257 morphology in cells devoid of STRN3 or of MAP4K4. STRIP1 has been associated with a contractile
258 motility mode, supporting migration in confined, stiff spaces[74]. Rounded, blebbing motility may contribute
259 to brain invasion, albeit at lower efficacy, and we previously observed a similar phenomenon in cells
260 treated with the SRC-BCR/ABL inhibitor dasatinib, which represses mesenchymal migration[75]. This

261 would explain why MAP4K4-depleted cells still display some invasiveness as MAP4K4 is mostly
262 involved in mesenchymal migration in MB cells. Together, our data indicate that co-operation of MAP4K4
263 and STRN3/4 favors filopodia formation through the induction of Ca^{2+}-activated kinases and the
264 phosphorylation of $VASP_{S157}$, which in concert with the previously identified regulation of ERM proteins
265 and the Arp2/3 complex by MAP4K4[17,27,28], promote invasive motility in environments of variable
266 complexity and stiffness.

267 In conclusion, we found that MAP4K4 exerts pro-invasive and anti-proliferative activities in MB cells
268 and that STRIPAK complex components contribute to and modulate these MAP4K4 functions
269 downstream of FGFR signaling. This dualism of MAP4K4 function in tumor cells provides an explanation
270 why MAP4K4 inhibition alone is not sufficient to shrink tumor volume *ex vivo,* despite its anti-invasive
271 activity. Remarkably however, co-depletion of MAP4K4 and STRN3 caused a near-complete eradication
272 of the tumor cells and completely abrogated cell dissemination *in vitro*. These findings argue strongly
273 for the development of STRN3 targeting strategies as therapeutic interventions to block MB cell
274 proliferation and invasion. Peptide disruption of the STRN3-PP2A interaction has anti-tumor effects by
275 impairing the phosphatase inactivation of the kinase in the complex and by activating the Hippo
276 pathway[50]. However, PP2A inhibition repressed invasion in MB cells in a dose-dependent manner,
277 indicating that STRIPAK-associated PP2A is rather unlikely to repress MAP4K4 pro-invasive activity
278 and that co-targeting of MAP4K4 and STRN3 or of their common downstream effectors such as nPKCs,
279 FAK and VASP could represent a successful strategy to impair both MB cell proliferation and spreading.
280 Phosphorylation status of these proteins in patient samples may inform clinicians in the future about the
281 potential susceptibility to therapies targeting this pathway.

282 Material and methods

283 *Reagents*

284 Protein phosphatase PP2A inhibitor LB-100 (S7537), PKC-θ inhibitor (S6577), Rottlerin (S7862), and
285 Bisindolylmaleimide I (S7208) were purchased from Selleckchem, Houston, TX, USA. MAP4K4 inhibitor
286 GNE-495 was kindly provided by Genentech Inc.[76]. EGF (100-47) and bFGF (100-18B) were purchased
287 from PeproTech, London, UK. If not otherwise indicated, the cells were treated with growth factors at
288 these concentrations*:* EGF: 30 ng/ml, bFGF: 100 ng/ml.

289 *Cells and cell culture*

290 DAOY human MB cells were purchased from the American Type Culture Collection (ATCC, Rockville,
291 MD, USA) and cultured in Iscove's Modified Dulbecco's Medium (IMEM, Sigma). HD-MBO3 group 3 MB
292 cells were generously provided by Till Milde (DKFZ, Germany) and cultured in RPMI medium (Sigma).
293 Human embryonic kidney HEK-293T cells were cultured in Dulbecco's modified Eagle's medium
294 (DMEM, Sigma). Cell culture media were supplemented with 10% fetal bovine serum (FBS, Sigma), 1%
295 Penicillin-Streptomycin (ThermoFisher Scientific), and 1% GlutaMAX (Gibco). DAOY LA-EGFP and HD-
296 MBO3 LA-EGFP cells were produced by lentiviral transduction of DAOY and HD-MBO3 cells with pLenti-
297 LA-EGFP. The cells were maintained at 37°C in a humidified atmosphere containing 5% CO_2. All cells
298 were confirmed to be mycoplasma negative. Cell line authentication and cross-contamination testing
299 were performed by Multiplexion by single nucleotide polymorphism (SNP) profiling.

300 ***Plasmids***

301 Lentiviral constructs were ordered from VectorBuilder (Santa Clara, CA, USA). For BioID experiments,
302 3xFLAG-tagged BioID2 biotin ligase was fused to either the N-terminus (3xFLAG-BioID2-MAP4K4) or
303 the C-terminus (MAP4K4-BioID2-3xFLAG) of human MAP4K4 cDNA (NM_145686.4). An extended
304 flexible linker consisting of 13 repeats of GGGGS was inserted between MAP4K4 and the BioID2
305 ligase[32]. As negative controls, only BioID2-FLAG was used. Details of the vectors can be found
306 at https://en.vectorbuilder.com/vector/VB180410-1463qqf.html (N-BioID-MAP4K4),
307 https://en.vectorbuilder.com/vector/VB180410-1356dmp.html (C-BioID2-MAP4K4), and
308 https://en.vectorbuilder.com/vector/VB180411-1121jky.html (BioID2-CTRL). See also Figure S1. For
309 the analysis of MAP4K4 domains, we designed different constructs encoding 3xFLAG-tagged truncated
310 versions of MAP4K4 cDNA (Figure 1j). Details of the vector can be found at:
311 https://en.vectorbuilder.com/vector/VB190724-1021fsg.html (full-length MAP4K4),
312 https://en.vectorbuilder.com/vector/VB190724-1072aza.html (ID1-ID2-CNH, residues 290-1273),
313 https://en.vectorbuilder.com/vector/VB190724-1048drb.html (KD, residues 1-289),
314 https://en.vectorbuilder.com/vector/VB190724-1089brg.html (KD-ID1-ID2, residues 1-954),
315 https://en.vectorbuilder.com/vector/VB190724-1058sct.html (ID1, residues 290-634), and
316 https://en.vectorbuilder.com/vector/VB190724-1062xrk.html (ID2, residues 635-954). All plasmids were
317 verified by Sanger sequencing.

318 ***Mouse maintenance***

319 Mouse protocols for organotypic brain slice culture were approved by the Veterinary Office of the Canton
320 Zürich (Approvals ZH134/17, ZH116/20). Wild type C57BL/6JRj pregnant females were purchased from
321 Janvier Labs and were kept in the animal facilities of the University of Zürich Laboratory Animal Center.

322 ***Immunoblotting (IB)***

323 To analyze total cell lysates by immunoblot, 1 x 10^5 DAOY wild type or 2.5 x 10^5 HD-MBO3 cells were
324 lysed using RIPA buffer supplemented with protease (Complete Mini, Roche) and phosphatase
325 inhibitors (PhosSTOP, Roche) and cleared by centrifugation. Protein concentration was assessed using
326 the Pierce BCA Protein Assay Kit (Thermo Fisher Scientific) according to the manufacturer's
327 instructions. Protein separation was performed on Mini-Protean TGX (4-15% or 4-20%) SDS-PAGE gel
328 (Bio-Rad) and transferred to PVDF membranes (Bio-Rad). After 1 h of blocking with 5% non-fat milk,
329 membranes were probed with primary antibodies listed in Supplementary material (Table 1). GAPDH or
330 β-tubulin were used as internal loading control. HRP-linked secondary antibodies (1:5000) were used
331 to detect the primary antibodies. Chemiluminescence detection was carried out using ChemiDoc Touch
332 Gel and Western Blot imaging system (Bio-Rad). The integrated density of immuno-reactive bands was
333 quantified using ImageJ (National Institutes of Health, USA).
334 To assess VASP S157 phosphorylation, the cells were seeded on a collagen-coated plate and starved
335 for 16 h before treatment with growth factor and inhibitors. Protein extraction was performed by directly
336 incubating the cells with a lysis buffer containing 2.5% SDS and 125 mM Tris-HCl (pH 6.8) at 95°C for
337 5 minutes. The lysates were resolved by SDS-PAGE and analyzed by IB as described above.

338 ***Biotin-streptavidin affinity purification***

339 The protocol for isolating proteins biotinylated by biotin ligase was adapted from the BioID method [32,34].
340 For proximity-labeling experiments with HEK-293T, 7 x 10^6 cells were transiently transfected with N-
341 BioID2-M4K4, C-BioID2-M4K4, or BioID2-CTRL plasmids using jetPRIME reagent (Polyplus
342 Transfection) according to manufacturers' instructions. Non-transfected WT HEK-293T cells were used
343 as a negative control (to exclude biotin-independent binders). Twenty-four hours after the transfection,
344 the cells were incubated with 50 µM biotin for 16 h. For proximity-labeling experiments with DAOY MB
345 cells, we generated cells stably transfected with N-BioID2-M4K4, C-BioID2-M4K4, or BioID2-CTRL
346 lentivirus. 5 x 10^6 cells were incubated with biotin as above. Parental WT DAOY cells were used as a
347 negative control. After 16 h of biotin incubation and two PBS washes, the cells were lysed at 4°C with 1

348 ml of lysis buffer containing 50 mM Tris-HCl (pH 7.5), 150 nM NaCl, 1 mM EDTA, 1 mM EGTA, 1%
349 Triton X-100, 0.1% SDS and protease inhibitor tablet (Roche). The protein concentrations were
350 normalized among the samples. Two mg of protein samples were incubated with 75 µl of pre-equilibrated
351 Dynabeads MyOne Streptavidin T1 magnetic beads (65602, Thermo Fisher Scientific) in low-binding
352 Eppendorf tubes. The mixtures were incubated for 3 h at 4 °C with end-over-end rotation. The beads
353 were collected using a magnetic rack and washed twice with lysis buffer and twice with 50 mM
354 ammonium bicarbonate (pH 8.3). 10% of the streptavidin-conjugated beads were used for
355 immunoblotting. Proteins were eluted by heating the beads at 95°C for 5 min in Laemmli Sample Buffer
356 (1610747, Bio-Rad) with 50 mM DTT followed by magnetic separation. The remaining beads with bound
357 proteins were transferred to a fresh centrifuge tube, resuspend in 150 µl of 50 mM ammonium
358 bicarbonate, and used for MS analysis. For each condition, three biological replicates were performed
359 and analyzed by MS.

360 ***Mass spectrometry (MS)***

361 Tryptic digestion of proteins isolated by streptavidin pull-down was performed based on the protocol
362 described in[33]. Data acquisition was performed by the Functional Genomics Center Zurich (FGCZ). In
363 brief, 50 µl of 8 M urea were added to 150 µl of bead-protein suspensions in 50 mM ammonium
364 bicarbonate (pH 8.3). Beads were reduced by adding 4 µl of 100 mM Tris (2-carboxyethyl) phosphine
365 (TCEP), alkylated with 4 µl of 500 mM chloroacetamide (CAA) and incubated at 30°C for 1 h in the dark
366 using an Eppendorf Thermomixer at 700 rpm. Sample volume was adjusted by adding 200 µl of digest
367 buffer (10 mM Tris-HCl, 2 mM $CaCl_2$, pH 8.2) to dilute the 8 M urea to 1 M before trypsin digestion. The
368 mixture was treated with 1 µg/sample trypsin and incubated for overnight digestion in the dark at 30°C
369 using an Eppendorf Thermomixer at 1000 rpm. The supernatant was collected in a fresh Eppendorf tube
370 after magnetic separation of the beads. The beads were washed twice with 100 µl 10 mM Tris-HCl pH
371 8.2/10% acetonitrile. These washes were pooled with the first eluate and acidified with 60 µl 5%
372 trifluoroacetic acid (TFA). The Samples were desalted on SepPack C18 (Thermo Fisher Scientific),
373 dried, and dissolved in 20 µl 0.1% formic acid. The samples were diluted 10-fold and transferred to
374 autosampler vials for liquid chromatography-tandem mass spectrometry (LC-MS/MS). 2 µl of samples
375 were injected. LC-MS/MS analysis was performed on an Orbitrap Fusion Tribrid Mass Spectrometer
376 (Thermo Fisher Scientific). Peptides were separated by Easy Nano LC 1000 liquid chromatography
377 (Thermo Fisher Scientific) at 0.3 ml/min flow rate interfaced to EASY-Spray Source (Thermo Fisher

378 Scientific). A trap column (Acclaim PepMap 100 C18) and an analytical column (EASY-Spray C18) were
379 used for separation. Peptides were eluted using an acetonitrile gradient.

380 ***Proteomic data analysis***

381 The MS/MS raw data of three biological replicates were combined and searched against a SwissProt
382 database with *Homo sapiens* taxonomy using Mascot (version 2.6.2, London, UK), with a parent ion
383 tolerance of 10 ppm and a fragment ion mass tolerance of 0.030 Da. The database was also expanded
384 with frequently observed contaminants, such as bovine serum albumin, trypsin, and keratins
385 carbamidomethylation of cysteine residues (C) was specified as a fixed modification and oxidation of
386 methionine (M) was set as a variable modification. Scaffold (version 4.8.9, Proteome Software Inc.,
387 Portland, OR) was used to validate MS/MS-based peptide and protein identifications. 1% and 0.1% false
388 discovery rate (FDR) cutoff on peptide and protein, respectively, was used to control for false
389 identifications. Protein identifications were accepted if they contained at least 2 identified peptides per
390 protein. Proteins that contained similar peptides and could not be differentiated based on MS/MS
391 analysis alone were grouped to satisfy the principles of parsimony. Proteins sharing significant peptide
392 evidence were grouped into clusters. Proteins detected in the parental control samples (WT cells lacking
393 BioID2 expression) were subtracted from the results. The significance of enrichment was tested using
394 a two-tailed student's *t*-test with equal variances. Hits were considered significantly enriched in
395 MAP4K4-BioID2 cells compared the unspecific background (BioID2-CTRL) if they had > 2-fold
396 enrichment and p-values < 0.05. Gene ontology (GO) enrichment analysis of MAP4K4-interacting
397 partners was performed using Metascape (http://metascape.org/) [77].

398 ***Co-immunoprecipitation (Co-IP)***

399 2.5 x 10^6 DAOY or 3.5 x 10^6 HEK-293T cells were lysed at 4°C with 400 µl of buffer containing 50 mM
400 Tris-HCl (pH 7.5), 150 nM NaCl, 0.3% NP-40 with protease and phosphatase inhibitor cocktail. Lysates
401 were cleared by centrifugation, and protein concentrations were normalized among the samples. For
402 immunoprecipitation, 30 µl of Dynabeads Protein G magnetic beads (10004D, Thermo Fisher Scientific)
403 were coated with 3 µg of anti-FLAG antibody by resuspending them in 60 µl PBS containing 0.02%
404 Tween-20 (P1379, Sigma), and rotated for 45 min at 4°C. 1 mg of protein samples was incubated with
405 the antibody-coated Dynabeads for 3 h at 4 °C with end-over-end rotation. The beads were washed four
406 times with TBS buffer (50 mM Tris-HCl pH 7.4, 150 mM NaCl). The proteins were eluted by incubating

407 the beads with 35 µl 100 µg/ml 3xFLAG-Peptide (F4799, Sigma Aldrich) at room temperature for 20 min
408 or by adding Laemmli Sample Buffer (1610747, Bio-Rad) containing 50 mM DTT and denaturation at
409 95°C for 5 min. The beads were then magnetically separated from the eluates and the samples analyzed
410 by IB as described above.

411 ***Immunofluorescence analysis (IFA)***

412 To visualize MAP4K4-BioID2 proteins, stably transduced DAOY cells were plated on glass coverslips
413 and incubated with 50 µM biotin for 16 h. The cells were fixed and permeabilized as described in[78]. The
414 fixed cells were incubated with Streptavidin Alexa Fluor 594 conjugate (Invitrogen) for 1.5 h at RT,
415 followed by incubation with primary antibodies overnight at 4°C. Secondary antibodies were incubated
416 for 2 h at RT.
417 For VASP localization analysis, 2000 LA-EGFP DAOY cells were seeded in a 384 well plate (781090,
418 Greiner Bio-One) coated overnight with 0.07 µg/µl collagen I (5005-B, Cell systems) diluted in 70%
419 EtOH. After seeding, the cells were starved for 16 h and treated with 100 ng/ml bFGF for 15 min. Cells
420 were fixed and incubated with primary and secondary antibodies as described above.
421 Imaging acquisition was performed using an SP8 confocal microscope (Leica). The list of the primary
422 and secondary antibodies used is provided in Supplementary material (Table 1).

423 ***Lentivirus Production and Transduction***

424 Lentiviral particles were produced by transfection of HEK-293T cells with transfer plasmids, psPAX2
425 (#12260, Addgene) and pCMV-VSV-G plasmids (#8454, Addgene)[79] in a ratio of 5:3:2 using
426 polyethylenimine (24765-2, Polysciences). Virus supernatant was harvested 30 h after transfection,
427 filtered, and concentrated using Amicon Ultra 15 ml Centrifugal Filters (Millipore). For the transduction,
428 human MB cells were incubated for 24 hours with supernatant containing the viral particles and 8
429 µg/ml polybrene. Two days after transduction, cells were selected with puromycin (DAOY: 2 µg/ml, HD-
430 MBO3: 1 µg/ml).

431 ***Generation of CRISPR/Cas9-mediated knockout cells***

432 Gene-specific single-guide RNA (sgRNAs) were designed using the online design tool at
433 https://design.synthego.com. Only highly specific target sites were selected, and the respective
434 sequences are listed in Supplementary material (Table 2). Oligonucleotides specific for the target sites
435 were synthesized with BsmBI restriction site overhangs by Microsynth (Balgach, Switzerland) and

436 cloned into the LentiCRISPRv2 transfer plasmid (Addgene plasmid #52961) with a single tube restriction
437 and ligation method as described in[80]. Production of lentiviral vectors and cell transduction was
438 performed as described above. The efficiency of the knockouts was tested by immunoblot.

439 ***RNA interference***

440 DAOY cells at approximately 70% confluency were transfected with DharmaFECT Transfection Reagent
441 4 (T-2004-03, Dharmacon) or Lipofectamine RNAiMAX Transfection Reagent (13778075, Thermo
442 Fisher Scientific) with 10 nM siRNAs following the manufacturer's instruction. The list of the siRNA used
443 is provided in Supplementary material (Table 3). Non-Targeting Control siRNA (siCTRL, D-001210-02-
444 05, Dharmacon) was used as a negative control for siRNA transfection. After 48 or 72 hours, RNA and
445 proteins were isolated from the cells to determine gene expression by qRT-PCR and to evaluate protein
446 expression by IB. For SIA, the cells were re-seeded to form spheroids in ultra-low adhesion plates 24 h
447 after the transfection.

448 ***RNA extraction and quantitative Real-Time PCR (qRT-PCR)***

449 Total RNA was isolated from cells with the RNeasy mini kit (74106, Qiagen). cDNA was obtained by
450 retro-transcription of 1 µg total RNA using High-capacity cDNA Reverse Transcription Kit (4368813,
451 Applied Biosystems). qRT-PCR was performed using PowerUp Syber Green (A25776, Thermo
452 Scientific) under conditions optimized for the 7900HT Fast Real-Time PCR System (Applied
453 Biosystems). The primers used were synthesized by Microsynth AG (Balgach, Switzerland). Primer
454 sequences are detailed in Supplementary material (Table 4). The relative expression levels of each
455 gene of interest were calculated using the $2^{-\Delta\Delta Ct}$ method normalized to 18s.

456 ***Spheroid invasion assay (SIA)***

457 SIA was performed and quantified according to[42]. In brief: 2500 cells/100 µl per well were seeded in
458 cell-repellent 96 well microplates (650970, Greiner Bio-One, Kremsmünster, Austria). The cells were
459 incubated at 37°C for 24 h to form spheroids. 70 µl medium was removed and replaced with 70 µl of a
460 solution containing 2.5% bovine collagen I (CellSystems, Troisdorf, Germany). Polymerized collagen I
461 hydrogels were overlaid with 100 µl of serum-free media containing growth factors and/or inhibitors 2x
462 concentrated. The cells were allowed to invade the collagen matrix for 24 h, after which they were
463 stained with Hoechst (1:2000, B2883, Sigma Aldrich) for 3-4 h. Images were acquired with an
464 AxioObserver 2 mot plus fluorescence microscope (Zeiss, Munich, Germany) or with an Operetta high-

465 content imaging system (PerkinElmer) at 5x magnification. When acquired with the Operetta
466 microscope, the spheroids were localized in the well by acquiring 3 z-planes with 250 µm z-spacing, re-
467 scanned by acquiring 16 z-planes with 25 µm z-spacing and a maximum intensity projection was
468 computed and used for further analysis. Cell invasion was determined as the sum of the distance
469 invaded by the cells from the center of the spheroid as quantified using an automated cell dissemination
470 counter (aCDc)[42] or using Harmony 4.5 software (PerkinElmer).

471 ***Colony formation assay***

472 DAOY (400 cells/well) or HD-MBO3 (600 cells/well) cells were seeded in a 6-well plate in complete
473 growth medium containing 10% FBS. The cells were allowed to adhere for 48 h, and the medium was
474 replaced with fresh growth medium containing 1% FBS ± GF. The cells were cultured at 37°C for 10
475 days (DAOY) or 15 days (HD-MBO3) with medium changes every third or fourth day. The colonies were
476 fixed in methanol for 10 min at -20°C and then stained with 0.5% crystal violet for 15 min. The number
477 and the area of the colonies were quantified by ImageJ using the plugin colony area.

478 ***CellTox green cytotoxicity assay***

479 Cytotoxicity was determined using the CellTox™ Green Cytotoxicity Assay (G8742, Promega,
480 Dübendorf, Switzerland), according to manufacturer's instructions. 2500 DAOY cells were seeded in
481 100 µl per well of complete medium in 96-well Corning black wall microplates with clear round bottom
482 (Corning Incorporated, NY, USA). The cells were incubated at 37°C for 24 h to form spheroids. 50 µl of
483 the medium were then removed from each well and replaced with 50 µL of fresh medium containing
484 1:500 of CellTox™ Green Dye and different drug concentrations. Wells with medium but without cells
485 were used to measure background fluorescence. The fluorescence representing nonviable cell was
486 measured after 24, 48, and 72 h of incubation using Cytation 3 imaging reader (BioTek, Sursee,
487 Switzerland) at Ex/Em 485/520 nm.

488 ***Ex vivo organotypic cerebellum slice culture (OCSC)***

489 Cerebellar slices were prepared from P8-10 C57BL/6JRj mouse pups as described in[47]. Slices were
490 kept in culture for 15 days. Medium was changed daily, and cultures monitored for signs of cell death.
491 Tumor spheroids from DAOY or HD-MBO3 LA-EGFP cells were used. For DAOY cells, the cells were
492 re-seeded to form spheroids in ultra-low adhesion plate 24 h after transfection with siRNA and implanted
493 on the slices 48 h after transfection. The slice-spheroid co-cultures were treated with EGF (30 ng/ml) or

494 bFGF (12.5 ng/ml) where indicated for 2 days (DAOY) or 5 days (HD-MBO3). Following the treatment,
495 the co-cultures were fixed and stained for calbindin, GFAP, or anti-human nuclei, as described in[47], and
496 analyzed using IFA. To evaluate the extent of proliferation both in the tumor cells and in the slice culture,
497 we performed 5-ethynyl-2′-deoxyuridine (EdU) staining using the Click-iT EdU Alexa Fluor 647 imaging
498 kit (C10340, Invitrogen). Four-color image acquisition was performed on an SP8 confocal microscope
499 (Leica). The perimeter and the area of the infiltrating spheroids, and the number of EdU-positive nuclei
500 were measured using ImageJ.

501 ***Patient gene expression and proteomic data***

502 Gene expression and proteomic data of pediatric brain tumor patients were obtained from the ProTrack
503 data portal (http://pbt.cptac-data-view.org/) from the Clinical Proteomic Tumor Analysis Consortium
504 (CPTAC) and the Children's Brain Tumor Tissue Consortium (CBTTC). The dataset used includes a
505 cohort of 218 tumor samples representing seven distinct histological diagnoses, including
506 medulloblastoma (MB), low-grade glioma (LGG), high-grade glioma (HGG), ependymoma (EP),
507 craniopharyngioma (CP), ganglioglioma (GG), and atypical teratoid rhabdoid tumor (ATRT)[41].

508 ***Protein kinase activity profiling***

509 4.5 x 10^5 DAOY cells were transfected with siRNA as described above. 72 h after the transfection and
510 O/N starvation, cells were stimulated with 100 ng/ml bFGF for 15 minutes and lysed in M-PER protein
511 extraction reagent (Thermo Fischer Scientific) supplemented with Halt Phosphatase Inhibitor Cocktail
512 and Halt Protease Inhibitor Cocktail EDTA free (Thermo Fischer Scientific). Lysates were cleared by
513 centrifugation, and protein concentrations were determined by Pierce BCA Protein Assay Kit (Thermo
514 Fisher Scientific). Aliquots of 1 mg/ml of lysates were prepared and snap-frozen in liquid nitrogen. Kinase
515 activity profiles were performed using the PamChip® serine/threonine (STK) and protein tyrosine (PTK)
516 peptide microarray system from PamGene ('s-Hertogenbosch, The Netherlands), according to standard
517 manufacturer's instructions. The PamChip® consists of 4 identical peptide arrays, each array containing
518 144 (STK) or 196 (PTK) peptides. The technology measures the phosphorylation of the arrayed STK
519 and PTK peptides and compares derived peptide phosphorylation signatures to known consensus
520 signatures of kinases to predict kinase activities. Three PamChip® microarrays were processed at the
521 same time on the PamStation®12 (PamGene). One and five µg of protein extract were used for the STK
522 array and the PTK array protocol, respectively, and the enzymatic assay was started by adding ATP

523 (final concentration 100 μM). For the PTK array, fluorescein isothiocyanate (FITC)–labeled pY20
524 antibody was incubated on the chip, and the phosphorylation of the individual Tyr peptides was followed
525 by fluorescence detection in real-time. For the STK array, the primary antibody mixture was incubated
526 with the chip, and the secondary FITC- conjugated antibody was used to quantify the signal. For each
527 condition, three biological replicates were performed and analyzed in three different runs.

528 ***Software and data analysis***

529 The fluorescent signal intensity for each peptide on the PamChip® was quantitated by BioNavigator
530 software (PamGene) and represented as linear regression slope as a function of exposure time. A local
531 background correction was used per spot. Nominal CV (Coefficient of variation) was calculated per
532 peptide with a 2-component error fit model, using the overall mean as input. Only peptides that showed
533 nominal CV <0.5 were included in the analysis. Additionally, Combat correction/normalization was
534 performed to correct for differences in batch effects. After averaging signal intensities across the 3
535 biological replicates per condition, the signal ratio between siTarget and siCTRL was used to calculate
536 fold change (FC) values. Peptides with a fold change of at least 35% (i.e., FC > 1.35 or FC < 0.65) were
537 considered differentially phosphorylated. To generate the peptide phosphorylation heatmap and
538 compare the global phosphorylation levels, the linear regression slope of each peptide was $\log_2$
539 transformed. Peptides differently phosphorylated ($p < 0.1$) in siTarget vs. siCTRL were identified by
540 ANOVA and postHoc Dunnett's tests. Venn diagram analyses were performed in Venny 2.1
541 (https://bioinfogp.cnb.csic.es/tools/venny/). An upstream kinase prediction tool based on the PamApp
542 on BioNavigator Analysis software was used to generate a putative list of kinases responsible for
543 phosphorylating the phosphosites on the PamChip. The prediction of the differentially activated
544 upstream kinases for each experimental group (siTarget vs. siCTRL, or bFGF vs. UT) is carried out by
545 a comparison of the phosphorylation sites of the peptides on the array with databases containing
546 experimental and literature-based protein modifications such as HPRD, PhosphoELM
547 (http://phospho.elm.eu.org), PhosphoSite Plus (https://www.phosphosite.org), Reactome
548 (http://reactome.org), UNIPROT (https://www.uniprot.org/) and in silico computational predictions
549 database such as PhosphoNet (http://www.phosphonet.ca/). The prediction tool functional rank-orders
550 the top kinases differentially activated between two compared groups. The mean kinase statistic
551 represents the difference in the predicted protein kinase activity between the two compared groups. A
552 positive value indicates an activation, while a negative value an inhibition. The specificity score indicates

553 the specificity of the normalized kinase statistics with respect to the number of peptides used for
554 predicting the corresponding kinase. The higher the specificity score, the higher is the power of the
555 prediction. Values of the specificity score >0.9 were considered as statistically relevant. To group the
556 kinases into sequence families, phylogenetic trees were created using the web-based kinome tool
557 CORAL (http://phanstiel-lab.med.unc.edu/CORAL/).

558 ***Statistical analysis***

559 Statistical analyses were performed using GraphPad Prism 8 software (San Diego, California).
560 Statistical significance of differences between groups was determined using Student's *t*-test (unpaired,
561 two-tailed) or one-way ANOVA repeated-measures test with Bonferroni's correction. The experiments
562 were performed in at least three independent biological replicates (n=3) unless differently indicated, and
563 results are shown as mean ± standard deviation (SD) or standard error of the mean (SEM). The results
564 were considered significant when $p < 0.05$ (*$p \leq 0.05$, ** $p \leq 0.01$, *** $p \leq 0.001$, **** $p \leq 0.0001$). Where
565 indicated, asterisks show statistical significances between control and test sample.

566 ## References

567 1. Hatten, M. E. & Roussel, M. F. Development and cancer of the cerebellum. *Trends Neurosci.* **34**,
568 134–142 (2011).

569 2. Cavalli, F. M. G. *et al.* Intertumoral Heterogeneity within Medulloblastoma Subgroups. *Cancer*
570 *Cell* **31**, 737--754.e6 (2017).

571 3. Schwalbe, E. C. *et al.* Novel molecular subgroups for clinical classification and outcome
572 prediction in childhood medulloblastoma: a cohort study. *Lancet Oncol.* **18**, 958–971 (2017).

573 4. Hovestadt, V. *et al.* Medulloblastomics revisited: biological and clinical insights from thousands
574 of patients. *Nat. Rev. Cancer* **20**, 42–56 (2020).

575 5. Gajjar, A. *et al.* Risk-adapted craniospinal radiotherapy followed by high-dose chemotherapy and
576 stem-cell rescue in children with newly diagnosed medulloblastoma (St Jude Medulloblastoma-
577 96): long-term results from a prospective, multicentre trial. *Lancet Oncol.* **7**, 813–820 (2006).

578 6. Gerber, N. U. *et al.* Recent developments and current concepts in Medulloblastoma. *Cancer*
579 *Treat. Rev.* **40**, 356–365 (2014).

580 7. Rieken, S. *et al.* Outcome and prognostic factors of radiation therapy for medulloblastoma. *Int.*
581 *J. Radiat. Oncol. Biol. Phys.* **81**, 7–13 (2011).

582 8. Wu, X. *et al.* Clonal selection drives genetic divergence of metastatic medulloblastoma. **482**,
583 529–533 (2012).

584 9. Santhana Kumar, K. *et al.* TGF-β Determines the Pro-migratory Potential of bFGF Signaling in
585 Medulloblastoma. *Cell Rep.* **23**, 3798-3812.e8 (2018).

586 10. Neve, A. *et al.* Crosstalk between SHH and FGFR signaling pathways controls tissue invasion in
587 medulloblastoma. *Cancers (Basel).* **11**, (2019).

588 11. Juraschka, K. & Taylor, M. D. Medulloblastoma in the age of molecular subgroups: A review. *J.*
589 *Neurosurg. Pediatr.* **24**, 353–363 (2019).

590 12. Friedl, P. & Wolf, K. Tumour-cell invasion and migration: diversity and escape mechanisms. *Nat.*
591 *Rev. Cancer* **3**, 362–374 (2003).

592 13. Lauffenburger, D. A. & Horwitz, A. F. Cell migration: A physically integrated molecular process.
593 *Cell* **84**, 359–369 (1996).

594 14. Ridley, A. J. *et al.* Cell Migration: Integrating Signals from Front to Back. *Science (80-.).* **302**,
595 1704–1709 (2003).

596 15. Makrilia, N., Kollias, A., Manolopoulos, L. & Syrigos, K. Cell adhesion molecules: Role and
597 clinical significance in cancer. *Cancer Invest.* **27**, 1023–1037 (2009).

598 16. Kumar, K. S. *et al.* The Ser/Thr kinase MAP4K4 drives c-Met-induced motility and invasiveness
599 in a cell-based model of SHH medulloblastoma. *Springerplus* **4**, 19 (2015).

600 17. MAP4K4 controlled integrin beta1 activation and c-Met endocytosis are associated with invasive
601 behavior of medulloblastoma cells. *Oncotarget* (2018).

602 18. Dan, I., Watanabe, N. M. & Kusumi, A. The Ste20 group kinases as regulators of MAP kinase
603 cascades. *Trends Cell Biol.* **11**, 220–230 (2001).

604 19. Su, Y. C., Han, J., Xu, S., Cobb, M. & Skolnik, E. Y. NIK is a new Ste20-related kinase that binds
605 NCK and MEKK1 and activates the SAPK/JNK cascade via a conserved regulatory domain.
606 *EMBO J.* **16**, 1279–1290 (1997).

607 20. Tesz, G. J. *et al.* Tumor Necrosis Factor α (TNFα) Stimulates Map4k4 Expression through TNFα
608 Receptor 1 Signaling to c-Jun and Activating Transcription Factor 2. *J. Biol. Chem.* **282**, 19302–
609 19312 (2007).

610 21. Tripolitsioti, D., Grotzer, M. A. & Baumgartner, M. The Ser/Thr Kinase MAP4K4 Controls Pro-
611 Metastatic Cell Functions. *J. Carcinog. Mutagen.* **08**, 1–8 (2017).

612 22. Roth Flach, R. J. *et al.* Endothelial protein kinase MAP4K4 promotes vascular inflammation and
613 atherosclerosis. *Nat. Commun.* **6**, (2015).

614 23. Danai, L. V *et al.* Inducible Deletion of Protein Kinase Map4k4 in Obese Mice Improves Insulin
615 Sensitivity in Liver and Adipose Tissues. *Mol. Cell. Biol.* **35**, 2356–2365 (2015).

616 24. Collins, C. S. *et al.* A small interfering RNA screen for modulators of tumor cell motility identifies
617 MAP4K4 as a promigratory kinase. *Proc. Natl. Acad. Sci.* **103**, 3775–3780 (2006).

618 25. Prolo, L. M. *et al.* Targeted genomic CRISPR-Cas9 screen identifies MAP4K4 as essential for
619 glioblastoma invasion. *Sci. Rep.* 1–12 (2019) doi:10.1038/s41598-019-50160-w.

620 26. Vitorino, P. *et al.* MAP4K4 regulates integrin-FERM binding to control endothelial cell motility.
621 *Nature* **519**, 425–430 (2015).

622 27. Baumgartner, M. *et al.* The Nck-interacting kinase phosphorylates ERM proteins for formation of
623 lamellipodium by growth factors. *Proc. Natl. Acad. Sci. U. S. A.* **103**, 13391–13396 (2006).

624 28. LeClaire, L. L., Rana, M., Baumgartner, M. & Barber, D. L. The Nck-interacting kinase NIK
625 increases Arp2/3 complex activity by phosphorylating the Arp2 subunit. *J. Cell Biol.* **208**, 161–
626 170 (2015).

627 29. Goudreault, M. *et al.* A PP2A Phosphatase High Density Interaction Network Identifies a Novel
628 Striatin-interacting Phosphatase and Kinase Complex Linked to the Cerebral Cavernous
629 Malformation 3. *Mol. Cell. proteomics* **8**, 157–171 (2009).

630 30. Chen, C. *et al.* Striatins Contain a Noncanonical Coiled Coil That Binds Protein Phosphatase 2A
631 A Subunit to Form a 2 : 2 Heterotetrameric Core of Striatin-interacting Phosphatase and Kinase
632 (STRIPAK) Complex *. *J. Biol. Chem.* **289**, 9651–9661 (2014).

633 31. Kück, U., Radchenko, D. & Teichert, I. STRIPAK , a highly conserved signaling complex , controls
634 multiple eukaryotic cellular and developmental processes and is linked with human diseases

635 Discovery of striatin. *Biol. Chem.* **400**, 1–18 (2019).

636 32. Kim, D. I. *et al.* An improved smaller biotin ligase for BioID proximity labeling. *Mol. Biol. Cell* **27**,
637 1188–1196 (2016).

638 33. Kim, D. I. *et al.* Probing nuclear pore complex architecture with proximity-dependent biotinylation.
639 *Proc. Natl. Acad. Sci.* 2453–2461 (2014) doi:10.1073/pnas.1406459111.

640 34. Roux, K. J., Kim, D. I., Raida, M. & Burke, B. A promiscuous biotin ligase fusion protein identifies
641 proximal and interacting proteins in mammalian cells. *J. Cell Biol.* **196**, 801–810 (2012).

642 35. Couzens, A. L. *et al.* Protein interaction network of the mammalian hippo pathway reveals
643 mechanisms of kinase-phosphatase interactions. *Sci. Signal.* **6**, (2013).

644 36. Seo, G. *et al.* MAP4K Interactome Reveals STRN4 as a Key STRIPAK Complex Component in
645 Hippo Pathway Regulation. *Cell Rep.* **32**, (2020).

646 37. Kim, J. W. *et al.* STRIPAK directs PP2A activity toward MAP4K4 to promote oncogenic
647 transformation of human cells. *Elife* **9**, 1–27 (2020).

648 38. Chen, R., Xie, R., Meng, Z., Ma, S. & Guan, K. L. STRIPAK integrates upstream signals to initiate
649 the Hippo kinase cascade. *Nat. Cell Biol.* **21**, (2019).

650 39. Hyodo, T. *et al.* Misshapen-like kinase 1 (MINK1) is a novel component of striatin-interacting
651 phosphatase and kinase (STRIPAK) and is required for the completion of cytokinesis. *J. Biol.*
652 *Chem.* **287**, 25019–25029 (2012).

653 40. Tang, Y. *et al.* Architecture, substructures, and dynamic assembly of STRIPAK complexes in
654 Hippo signaling. *Cell Discov.* **5**, (2019).

655 41. Petralia, F. *et al.* Integrated Proteogenomic Characterization across Major Histological Types of
656 Pediatric Brain Cancer. *Cell* **183**, 1962--1985.e31 (2020).

657 42. Kumar, K. S. *et al.* Computer-assisted quantification of motile and invasive capabilities of cancer
658 cells. *Sci. Rep.* **5**, 15338 (2015).

659 43. Gordon, J. *et al.* Protein phosphatase 2a (PP2A) binds within the oligomerization domain of
660 striatin and regulates the phosphorylation and activation of the mammalian Ste20-Like kinase
661 Mst3. *BMC Biochem.* **12**, 1–18 (2011).

662 44. Zheng, Y. *et al.* Homeostatic Control of Hpo/MST Kinase Activity through Autophosphorylation-
663 Dependent Recruitment of the STRIPAK PP2A Phosphatase Complex. *Cell Rep.* **21**, 3612–3623
664 (2017).

665 45. Ho, W. S. *et al.* PP2A inhibition with LB100 enhances cisplatin cytotoxicity and overcomes
666 cisplatin resistance in medulloblastoma cells. *Oncotarget* **7**, 12447–12463 (2016).

667 46. Yang, D., Okamura, H., Morimoto, H., Teramachi, J. & Haneji, T. Protein phosphatase 2A C $α$
668 regulates proliferation , migration , and metastasis of osteosarcoma cells. *Lab. Investig.* **96**,
669 1050–1062 (2016).

670 47. Neve, A., Kumar, K. S., Tripolitsioti, D., Grotzer, M. A. & Baumgartner, M. Investigation of brain
671 tissue infiltration by medulloblastoma cells in an ex vivo model. *Sci. Rep.* **7**, (2017).

672 48. Meng, Z. *et al.* MAP4K family kinases act in parallel to MST1/2 to activate LATS1/2 in the Hippo
673 pathway. *Nat. Commun.* **6**, 1–13 (2015).

674 49. Zheng, Y. *et al.* Identification of Happyhour/MAP4K as Alternative Hpo/Mst-like Kinases in the
675 Hippo Kinase Cascade. *Dev. Cell* **34**, 642–655 (2015).

676 50. Tang, Y. *et al.* Selective Inhibition of STRN3-Containing PP2A Phosphatase Restores Hippo
677 Tumor-Suppressor Activity in Gastric Cancer. *Cancer Cell* 1–14 (2020)
678 doi:10.1016/j.ccell.2020.05.019.

679 51. Ribeiro, P. S. *et al.* Combined Functional Genomic and Proteomic Approaches Identify a PP2A
680 Complex as a Negative Regulator of Hippo Signaling. *Mol. Cell* **39**, 521–534 (2010).

681 52. Gschwendt, M. *et al.* Rottlerin, a novel protein kinase inhibitor. *Biochemical and Biophysical*
682 *Research Communications* vol. 199 93–98 (1994).

683 53. Cywin, C. L. *et al.* Discovery of potent and selective PKC-θ inhibitors. *Bioorganic Med. Chem.*
684 *Lett.* **17**, 225–230 (2007).

685 54. Mohammadi, M. *et al.* A tyrosine-phosphorylated carboxy-terminal peptide of the fibroblast
686 growth factor receptor (Flg) is a binding site for the SH2 domain of phospholipase C-gamma 1.
687 *Mol. Cell. Biol.* **11**, 5068–5078 (1991).

688 55. Chen, R. *et al.* Regulation of Akt/PKB Activation by Tyrosine Phosphorylation. *J. Biol. Chem.*
689 **276**, 31858–31862 (2001).

690 56. Skoble, J., Auerbuch, V., Goley, E. D., Welch, M. D. & Portnoy, D. A. Pivotal role of VASP in
691 Arp2/3 complex-mediated actin nucleation, actin branch-formation, and Listeria monocytogenes
692 motility. *J. Cell Biol.* **155**, 89–100 (2001).

693 57. Barzik, M. *et al.* Ena/VASP proteins enhance actin polymerization in the presence of barbed end
694 capping proteins. *J. Biol. Chem.* **280**, 28653–28662 (2005).

695 58. Benz, P. M. *et al.* Differential VASP phosphorylation controls remodeling of the actin
696 cytoskeleton. *J. Cell Sci.* **122**, 3954–3965 (2009).

697 59. Harbeck, B., Hüttelmaier, S., Schlüter, K., Jockusch, B. M. & Illenberger, S. Phosphorylation of
698 the vasodilator-stimulated phosphoprotein regulates its interaction witn actin. *J. Biol. Chem.* **275**,
699 30817–30825 (2000).

700 60. Lu, J. *et al.* MEKK2 and MEKK3 orchestrate multiple signals to regulate Hippo pathway. *J. Biol.*
701 *Chem.* **95**, 106408 (2021).

702 61. Garg, R. *et al.* Protein kinase C and cancer: What we know and what we do not. *Oncogene* **33**,
703 5225–5237 (2014).

704 62. Du, Q. Y. *et al.* High STRN Expression Promotes HCC Invasion and Migration but Not Cell
705 Proliferation or Apoptosis through Facilitating Epithelial-Mesenchymal Transition. *Biomed Res.*
706 *Int.* **2020**, (2020).

707 63. Wong, M. *et al.* Silencing of STRN4 suppresses the malignant characteristics of cancer cells.
708 *Cancer Sci.* **105**, 1526–1532 (2014).

709 64. Lee, T. H. *et al.* Rottlerin, a natural polyphenol compound, inhibits upregulation of matrix
710 metalloproteinase-9 and brain astrocytic migration by reducing PKC-$δ$-dependent ROS signal.
711 *J. Neuroinflammation* **17**, 1–13 (2020).

712 65. Sarkar, S. & Yong, V. W. Reduction of protein kinase C delta attenuates tenascin-C stimulated
713 glioma invasion in three-dimensional matrix. *Carcinogenesis* **31**, 311–317 (2010).

714 66. Brenner, W. *et al.* Migration of renal carcinoma cells is dependent on protein kinase Cδ via β1
715 integrin and focal adhesion kinase. *Int. J. Oncol.* **32**, 1125–1131 (2008).

716 67. Cannon, J. L. *et al.* PKCθ regulates T cell motility via ezrin-radixin-moesin localization to the
717 uropod. *PLoS One* **8**, (2013).

718 68. Madaro, L. *et al.* PKCθ signaling is required for myoblast fusion by regulating the expression of
719 caveolin-3 and β1D integrin upstream focal adhesion kinase. *Mol. Biol. Cell* **22**, 1409–1419
720 (2011).

721 69. Döppler, H. & Storz, P. Regulation of VASP by phosphorylation Consequences for cell migration.
722 *Cell Adhes. Migr.* **7**, 482–486 (2013).

723 70. Hasegawa, Y., Murph, M., Yu, S., Tigyi, G. & Mills, G. B. Lysophosphatidic acid (LPA)-induced
724 vasodilator-stimulated phosphoprotein mediates lamellipodia formation to initiate motility in PC-
725 3 prostate cancer cells. *Mol. Oncol.* **2**, 54–69 (2008).

726 71. Heckman, C. A. & Plummer, H. K. Filopodia as sensors. *Cell. Signal.* **25**, 2298–2311 (2013).

727 72. Jacquemet, G., Hamidi, H. & Ivaska, J. Filopodia in cell adhesion, 3D migration and cancer cell
728 invasion. *Curr. Opin. Cell Biol.* **36**, 23–31 (2015).

729 73. Steketee, M. B. & Tosney, K. W. Three functionally distinct adhesions in filopodia: Shaft
730 adhesions control lamellar extension. *J. Neurosci.* **22**, 8071–8083 (2002).

731 74. Madsen, C. D. *et al.* STRIPAK components determine mode of cancer cell migration and
732 metastasis. *Nat. Cell Biol.* **17**, 68–80 (2015).

733 75. Schönholzer, M. T. *et al.* Real-time sensing of MAPK signaling in medulloblastoma cells reveals
734 cellular evasion mechanism counteracting dasatinib blockade of ERK activation during invasion.
735 *Neoplasia* **22**, 470–483 (2020).

736 76. Ndubaku, C. O. *et al.* Structure-Based Design of GNE-495, a Potent and Selective MAP4K4
737 Inhibitor with Efficacy in Retinal Angiogenesis. *ACS Med. Chem. Lett.* **6**, 913–918 (2015).

738 77. Zhou, Y. *et al.* Metascape provides a biologist-oriented resource for the analysis of systems-level
739 datasets. *Nat. Commun.* **10**, (2019).

740 78. Ma, M. & Baumgartner, M. Intracellular Theileria annulata Promote Invasive Cell Motility through
741 Kinase Regulation of the Host Actin Cytoskeleton. *PLoS Pathog.* **10**, e1004003--4 (2014).

742 79. Stewart, S. A. *et al.* Lentivirus-delivered stable gene silencing by RNAi in primary cells. *Rna* **9**,
743 493–501 (2003).

744 80. McComb, S. *et al.* Activation of concurrent apoptosis and necroptosis by SMAC mimetics for the

745 treatment of refractory and relapsed ALL. *Sci. Transl. Med.* **8**, (2016).

746 81. Jeong, B. *et al.* Cryo-EM structure of the Hippo signaling integrator human STRIPAK. *Nat. Struct.*
747 *Mol. Biol.* 1–10 (2021) doi:10.1038/s41594-021-00564-y.

748 82. Varnaitė, R. & MacNeill, S. A. Meet the neighbors: Mapping local protein interactomes by
749 proximity-dependent labeling with BioID. *Proteomics* **16**, 2503–2518 (2016).

750

751 ## Acknowledgments

752 The authors thank Dr. Savithri Rangarajan (PamGene International) for scientific support and analysis
753 of PamChip imaging data and Dr. Jens Sobek (Functional Genomics Center Zurich) for assistance with
754 the experiments performed on PamStation®12. We would like to thank members of the Functional
755 Genomics Center Zurich for mass spectrometry support. Imaging was performed with equipment
756 maintained by the Centre for Microscopy and Image Analysis, University of Zurich. This study was
757 supported by grants from the Swiss National Science foundation (SNF_31003A_165860/1,
758 SNF_310030_188793) and the Swiss Cancer League (SCL_KLS-3834-02-2016) to MB, the University
759 of Zürich (Candoc) to J.M. and from the Childhood Cancer Foundation to MG.

760 ## Author contributions

761 J.M. contributed to designing the study, planned and conducted all the experiments, prepared the
762 figures, and wrote the manuscript. B.S. generated DAOY cells stably expressing different MAP4K4
763 domains. C.C. provided experimental support for image acquisition and quantification with the Operetta
764 microscope. M.G. helped to draft the study. M.B. designed the study and wrote the manuscript.

765

766 ## Figures

767 **Figure 1: BioID identifies MAP4K4-STRIPAK complex interaction in MB cells. (a**) Immunoblot
768 analysis (IB) of HEK-293T total cell lysate or after immunoprecipitation (IP) with streptavidin-conjugated
769 beads and detection with HRP-streptavidin. *n*=2 experiments. **(b)** Venn diagram of affinity captured
770 proteins from HEK-293T cells. Comparison of BioID2-MAP4K4 with BioID2-CTRL is shown. Values of
771 enriched proteins ($p < 0.05$, one-way ANOVA) are shown. *n*=3. **(c)** Gene ontology (GO) classifications
772 of MAP4K4-interacting proteins. **(d)** Volcano plot of interacting proteins in N-BioID2-MAP4K4 (left) or C-
773 BioID2-MAP4K4 (right) HEK-293T cells compared to BioID2-CTRL. Log_{10} ratios of cumulated peptide
774 detection values plotted against negative Log_{10} p-values of Student's *t*-test. Enriched proteins are

775 highlighted in red ($p < 0.05$ and > 2-fold enrichment) and members of the STRIPAK complex indicated.
776 **(e)** Architecture of the STRIPAK complex, adapted from[81]. **(f)** IB detection of BioID2-MAP4K4-FLAG and
777 components of STRIPAK complex in anti-FLAG-IP in HEK-293T cells. **(g)** IB of FLAG-tagged BioID2
778 alone or fused to MAP4K4 in DAOY cell lysate or after pull-down with streptavidin-conjugated beads.
779 **(h)** Venn diagram of affinity-captured proteins from DAOY BioID2-MAP4K4 cells compared to BioID2-
780 CTRL. *n*=2. **(I)** IB of MAP4K4-FLAG and components of STRIPAK complex after anti-FLAG-IP in DAOY
781 cells. **(j)** Top: MAP4K4 domain architecture and MAP4K4 constructs used. Numbers represent the
782 amino acids corresponding to full-length MAP4K4. KD, kinase domain; ID, intermediate domain; CNH,
783 citron homology domain; CC, coiled-coil. Lower: Co-IP and IB analysis of STRN4 and STRIP1 in DAOY
784 cells transduced with lentiviral vectors expressing full-length or truncated MAP4K4-FLAG. Asterisks
785 indicate relevant bands. **(k)** Quantification of co-IP from **j** (*n*=3, means ± SD). See also Figure S1.
786

787 **Figure 2: STRIPAK complex disruption impairs GF-induced collagen I invasion. (a)** Invasion and
788 representative images of 3D spheroid invasion assay (SIA) of DAOY cells KO for MAP4K4, STRN4,
789 STRN3, or STRIP1 ± bFGF (100 ng/ml). Invasion is calculated as sum of the distances of each migrating
790 cell from the center of the spheroids (*n*=3, means ± SD). **(b)** SIA of DAOY cells transfected with 10 nM
791 of the indicated siRNA ± GFs (EGF: 30 ng/ml, bFGF: 100 ng/ml). *n*=4, means ± SD. **(c)** SIA and
792 representative images of DAOY cells ± 100 ng/ml bFGF and ± increasing concentrations of PP2A
793 inhibitor LB-100 (*n*=3, means ± SD). * $p < 0.05$, ** $p < 0.01$, *** $p < 0.001$, **** $p < 0.0001$ (one-way
794 ANOVA). See also Figure S3.
795

796 **Figure 3: Depletion of MAP4K4 and STRN3 blocks tissue invasion in SHH MB cell model. (a)**
797 Timeline of organotypic cerebellum slice culture (OCSC) and tumor spheroid implantation. **(b)** Maximum
798 intensity projections (MIP) of representative confocal sections of OCSCs implanted with DAOY tumor
799 cell spheroids ± 30 ng/ml EGF for 48h. Green: Lifeact-EGFP; blue: calbindin (Purkinje cells); red: GFAP.
800 Middle: Inverted greyscale images of MIP of LA-EGFP channel, lower: Inverted greyscale images of
801 MIP of EdU-Click-IT staining. Scale bar: 200 µm. **(c)** Quantification of LA-EGFP area of spheroids shown
802 in **b** (*n*=3, means ± SD). **(d)** Number of EdU-positive nuclei normalized by the area of the tumor
803 spheroids (*n*=3, means ± SD). * $p < 0.05$, ** $p < 0.01$, *** $p < 0.001$ (unpaired Student's *t*-test). See also
804 Figure S4.
805 **Figure 4: STRN3 is necessary for invasive growth of group 3 MB cell model in cerebellar tissue.**
806 **(a)** Organotypic cerebellum slice culture implanted with tumor spheroids derived from HD-MBO3 cells
807 KO for MAP4K4, STRN4, STRN3, or STRIP1. MIP of representative slices five days after implantation
808 and ± treatment with 30 ng/ml EGF or 12.5 ng/ml bFGF. Green: Lifeact-EGFP; blue: calbindin (Purkinje
809 cells); red: GFAP; yellow: Edu-Click-IT. Scale bar: 200 µm. **(b)** Areas of LA-EGFP positive spheroids
810 showed in **a**. *n*=3, means ± SD. **(c)** Number of EdU-positive nuclei normalized by the area in pixels of
811 the tumor spheroids (*n*=3, means ± SD). * $p < 0.05$, ** $p < 0.01$, *** $p < 0.001$, **** $p < 0.0001$ (unpaired
812 Student's *t*-test). See also Figure S5.
813

814 **Figure 5: STRN4/3 and MAP4K4 display opposing functions towards MB cell proliferation, clonal**
815 **growth and YAP/TAZ target gene expression. (a)** Colony formation assay of DAOY cells KO for
816 MAP4K4, STRN4, STRN3, or STRIP1 ± EGF or bFGF treatment (EGF: 30 ng/ml, bFGF: 100 ng/ml).
817 Representative images (left) and quantification (right, *n*=3, means ± SD). **(b)** Colony formation assay
818 using HD-MBO3 cells with treatments as in a. (*n*=3, means ± SD). **(c)** qRT-PCR analysis of YAP/TAZ
819 target genes in DAOY cells 48 h after transfection with siRNAs as indicated. *n*=4, means ± SD. **(d)** qRT-
820 PCR analysis of YAP/TAZ target genes in HD-MBO3 with CRISPR/Cas9-mediated knockout of
821 MAP4K4, STRN4, STRN3, or STRIP1 (*n*=3, means ± SD). Statistical analyses in **a** and **b** were
822 performed by one-way ANOVA, in **c** and **d** by unpaired Student's *t*-test. * $p < 0.05$, ** $p < 0.01$, *** $p <$
823 0.001, **** $p < 0.0001$. See also Figure S6.
824

825 **Figure 6: Novel protein kinases C are pro-migratory effectors of MAP4K4 and STRN3. (a)** Kinase
826 activity prediction analysis in DAOY cells transfected with the indicated siRNAs and ± stimulation with
827 100 ng/ml bFGF for 15 min. The plots show predicted top 25 differentially activated serine/threonine
828 kinases (STK). The x-axis indicates differences in the activity of the predicted protein kinase between
829 the two groups, with effect size (values) and direction (>0=activation; <0=inhibition). The color of the
830 bars represents the specificity score (darker to light is higher to lower score). Values >0.9 were

831 considered as statistically relevant. First graph from left: comparison of bFGF stimulated siCTRL cells
832 vs. untreated (UT); all other graphs: comparison of the indicated siTarget vs. siCTRL with bFGF
833 stimulation. Highlighted in red are novel PKC isoforms (δ, ε, η and θ) (*n*=3). **(b-e)** Quantification and
834 representative images of SIA with DAOY cells stimulated with 100 ng/ml bFGF and treated with
835 increasing concentrations of PKC inhibitors. Invasion was quantified as the sum of invasion distances
836 from the center of the spheroids. **b:** Rottlerin (PKCδ inhibitor, *n*=4, means ± SD). **c:** PKCθ inhibitor (*n*=4,
837 means ± SD). **d:** Combination of Rottlerin and PKCθ inhibitor (*n*=3, means ± SD). **e:** Bisindolylmaleimide
838 I (BIM, PKCα/β/γ inhibitor, *n*=4, means ± SD). * $p < 0.05$, ** $p < 0.01$, **** $p < 0.0001$ (one-way ANOVA).
839 See also Figure S7.
840

841 **Figure 7: MAP4K4 and STRN3 mediate VASP$_{S157}$ phosphorylation. (a)** Heat map of increased (red)
842 and decreased (blue) phosphorylation of Ser/Thr (STK, left) or Tyr (PTK, right) consensus peptides
843 associated with lysates from siRNA transfected DAOY cells treated ± 100 ng/ml bFGF for 15 min. Log_2
844 of the fold change between siTarget and siCTRL (*n*=3). **(b)** Venn diagram displaying the number of
845 Ser/Thr and Tyr peptides with significantly changed phosphorylation ($p < 0.1$) in each siTarget versus
846 siCTRL with bFGF stimulation (*n*=3). **(c)** Volcano plots representing the changes in phosphorylation of
847 STK (circles) and PTK (diamonds) peptides in siMAP4K4 (left) or siSTRN3 (right) versus siCTRL with
848 bFGF stimulation. Blue: peptides with significantly decreased (fold change < 1.35), red: peptides with
849 significantly increased phosphorylation (fold change > 1.35). (*n*=3). See also Figure S8 and Table S3.
850 **(d)** Single confocal section of VASP localization in DAOY cells seeded on collagen-coated plates ± 100
851 ng/ml bFGF for 15 min. 3X magnifications of boxed areas are shown. Red: VASP, Green: Lifeact-EGFP.
852 Blue: DNA (Hoechst). Scale bar: 20 µm. **(e)** Maximum intensity projection of LA-EGFP fluorescence of
853 tissue-invading HD-MBO3 CTRL or KO MAP4K4 or STRN3 cells. Scale bar: 10 µm. **(f)** IB and
854 quantification of VASP$_{S157}$ phosphorylation in DAOY cells 72 h after siRNA transfection ± 100 ng/ml
855 bFGF for 15 min (*n*=3, means ± SD). **(g-h)** IB and quantification of VASP$_{S157}$ phosphorylation in DAOY
856 **(g)** and HD-MBO3 cells **(h)** after treatment for 4 h with increasing concentration of GNE-495 ± 100 ng/ml
857 bFGF for 15 min. Quantification represents the ratio of p-VASP$_{S157}$ over total VASP relative to untreated
858 control (**g**: *n*=3, means ± SD. **h:** *n*=2, means ± SD). **(i)** Model for MAP4K4 and STRIPAK regulation of
859 PKC and p-VASP$_{S157}$ and its putative implication in filopodia formation.

Figure 1

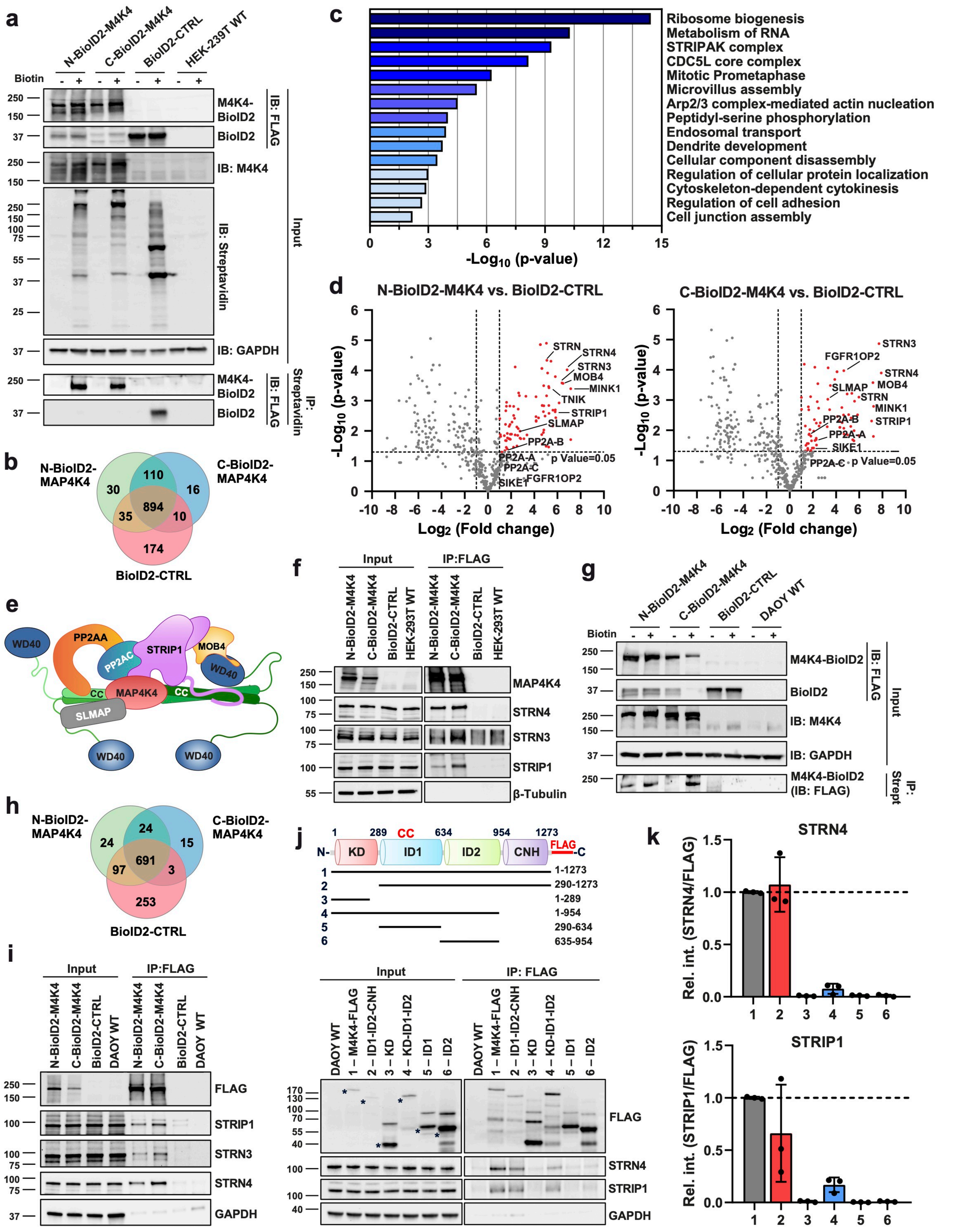
a
N-BioID2-M4K4
C-BioID2-M4K4
BioID2-CTRL
HEK-239T WT
Biotin
M4K4-BioID2
BioID2
IB: FLAG
IB: M4K4
IB: Streptavidin
IB: GAPDH
Input
IP: Streptavidin
b
N-BioID2-MAP4K4
C-BioID2-MAP4K4
BioID2-CTRL
110
30
16
894
35
10
174
c
Ribosome biogenesis
Metabolism of RNA
STRIPAK complex
CDC5L core complex
Mitotic Prometaphase
Microvillus assembly
Arp2/3 complex-mediated actin nucleation
Peptidyl-serine phosphorylation
Endosomal transport
Dendrite development
Cellular component disassembly
Regulation of cellular protein localization
Cytoskeleton-dependent cytokinesis
Regulation of cell adhesion
Cell junction assembly
-Log10 (p-value)
d
N-BioID2-M4K4 vs. BioID2-CTRL
C-BioID2-M4K4 vs. BioID2-CTRL
-Log10 (p-value)
Log2 (Fold change)
p Value=0.05
STRN
STRN4
STRN3
MOB4
MINK1
TNIK
STRIP1
SLMAP
PP2A-B
PP2A-A
PP2A-C
SIKE1
FGFR1OP2
e
WD40
PP2AA
PP2AC
STRIP1
MOB4
WD40
CC
MAP4K4
CC
SLMAP
WD40
WD40
f
Input
IP:FLAG
N-BioID2-M4K4
C-BioID2-M4K4
BioID2-CTRL
HEK-293T WT
MAP4K4
STRN4
STRN3
STRIP1
β-Tubulin
g
N-BioID2-M4K4
C-BioID2-M4K4
BioID2-CTRL
DAOY WT
Biotin
M4K4-BioID2
BioID2
IB: FLAG
IB: M4K4
IB: GAPDH
Input
M4K4-BioID2 (IB: FLAG)
IP: Strept
h
N-BioID2-MAP4K4
C-BioID2-MAP4K4
BioID2-CTRL
24
24
15
691
97
3
253
i
Input
IP:FLAG
N-BioID2-M4K4
C-BioID2-M4K4
BioID2-CTRL
DAOY WT
FLAG
STRIP1
STRN3
STRN4
GAPDH
j
1
289
CC
634
954
1273
N-
KD
ID1
ID2
CNH
FLAG
-C
1-1273
290-1273
1-289
1-954
290-634
635-954
Input
IP: FLAG
DAOY WT
1 – M4K4-FLAG
2 – ID1-ID2-CNH
3 – KD
4 – KD-ID1-ID2
5 – ID1
6 – ID2
FLAG
STRN4
STRIP1
GAPDH
k
STRN4
STRIP1
Rel. int. (STRN4/FLAG)
Rel. int. (STRIP1/FLAG)

Figure 2

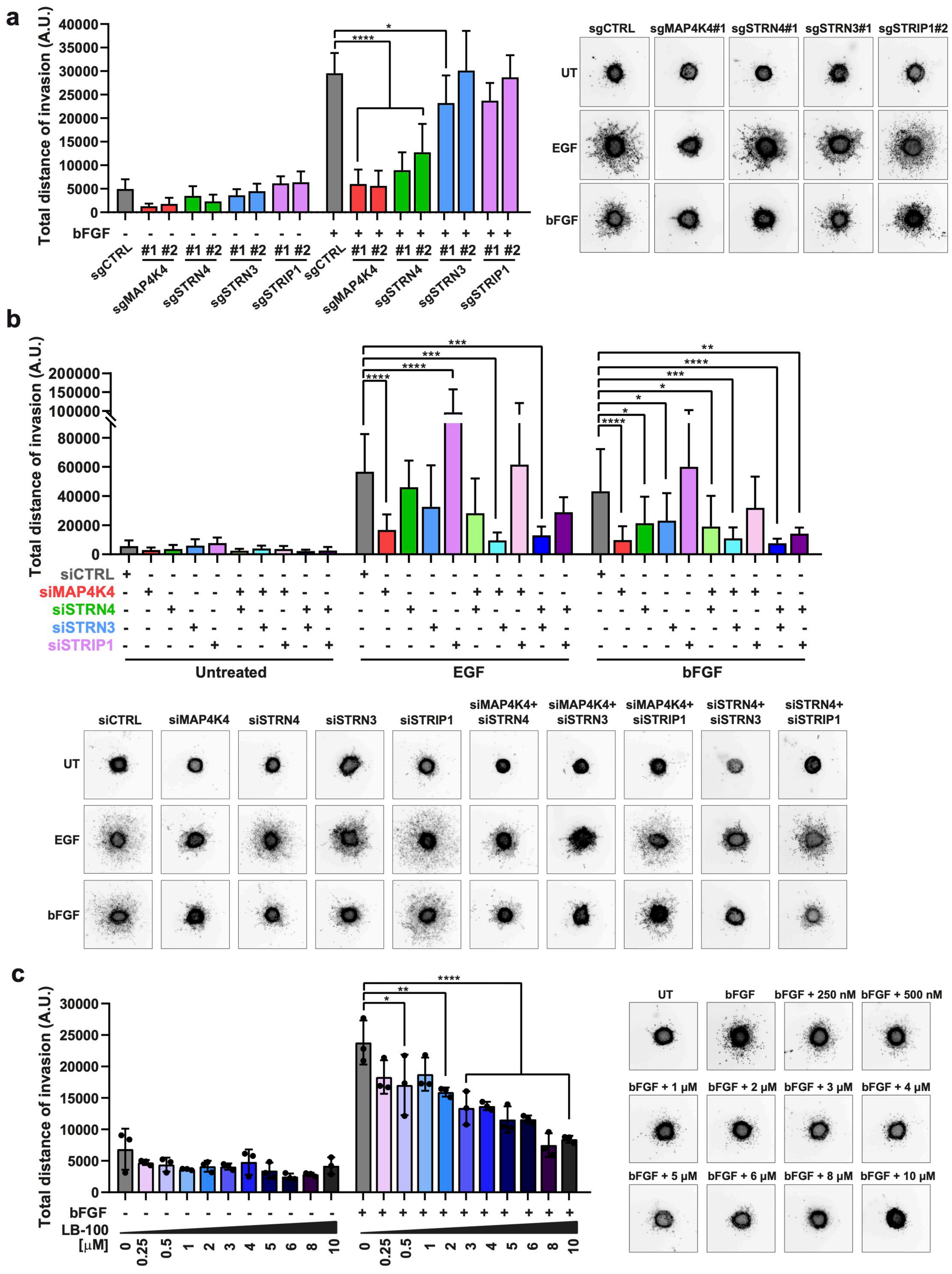
a
Total distance of invasion (A.U.)
bFGF
sgCTRL
sgMAP4K4
sgSTRN4
sgSTRN3
sgSTRIP1
#1 #2
sgCTRL sgMAP4K4#1 sgSTRN4#1 sgSTRN3#1 sgSTRIP1#2
UT
EGF
bFGF
b
Total distance of invasion (A.U.)
siCTRL
siMAP4K4
siSTRN4
siSTRN3
siSTRIP1
Untreated
EGF
bFGF
siCTRL siMAP4K4 siSTRN4 siSTRN3 siSTRIP1 siMAP4K4+ siSTRN4 siMAP4K4+ siSTRN3 siMAP4K4+ siSTRIP1 siSTRN4+ siSTRN3 siSTRN4+ siSTRIP1
UT
EGF
bFGF
c
Total distance of invasion (A.U.)
bFGF
LB-100 [μM]
UT bFGF bFGF + 250 nM bFGF + 500 nM
bFGF + 1 μM bFGF + 2 μM bFGF + 3 μM bFGF + 4 μM
bFGF + 5 μM bFGF + 6 μM bFGF + 8 μM bFGF + 10 μM

Figure 3

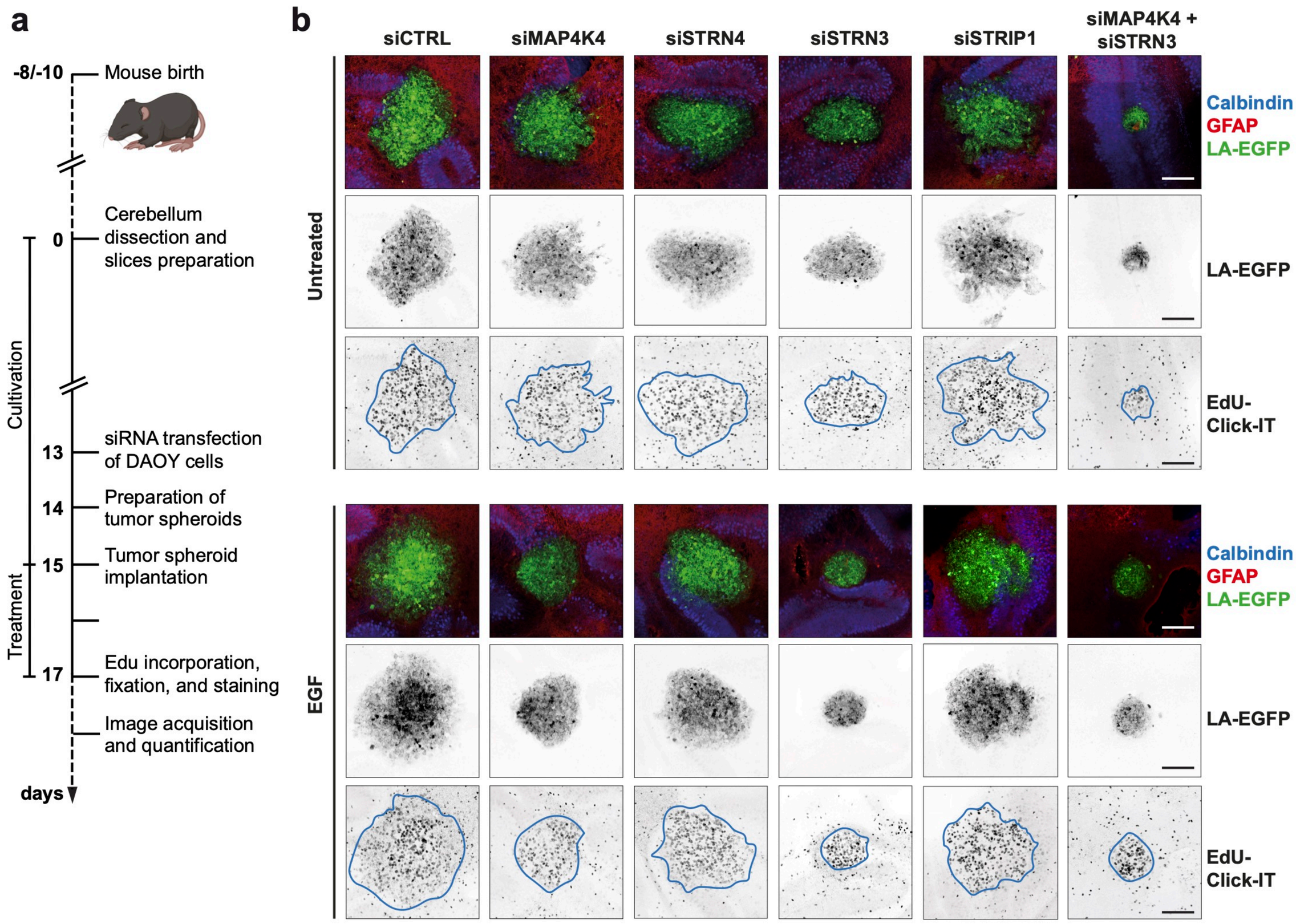
a
-8/-10
Mouse birth
0
Cerebellum dissection and slices preparation
Cultivation
13
siRNA transfection of DAOY cells
14
Preparation of tumor spheroids
15
Tumor spheroid implantation
Treatment
17
Edu incorporation, fixation, and staining
Image acquisition and quantification
days
b
siCTRL
siMAP4K4
siSTRN4
siSTRN3
siSTRIP1
siMAP4K4 + siSTRN3
Untreated
EGF
Calbindin
GFAP
LA-EGFP
LA-EGFP
EdU-Click-IT

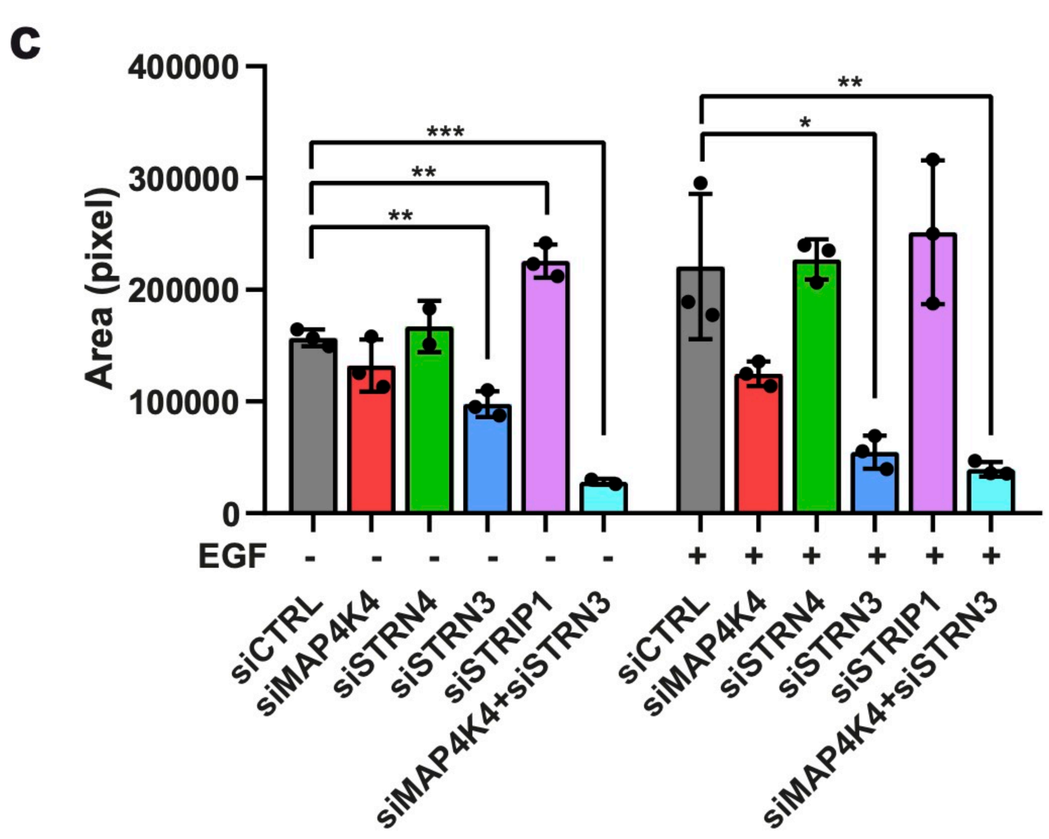
c
Area (pixel)
400000
300000
200000
100000
0
***
**
**
**
*
EGF
siCTRL
siMAP4K4
siSTRN4
siSTRN3
siSTRIP1
siMAP4K4+siSTRN3

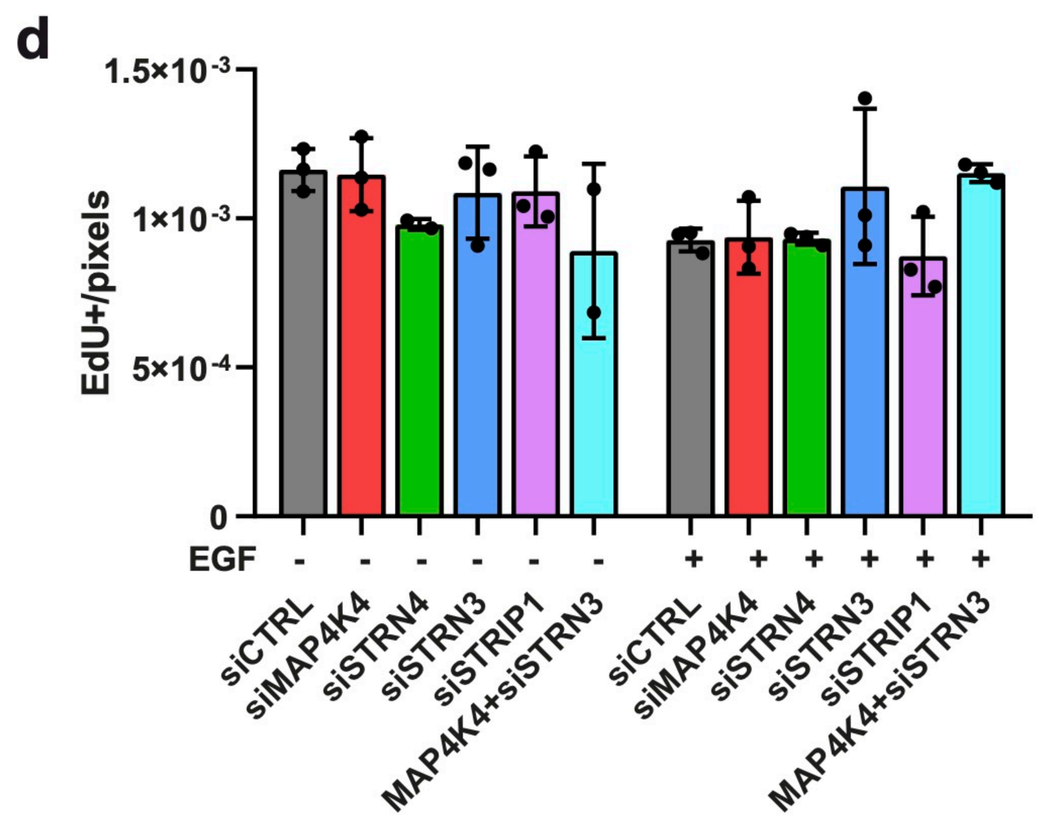
d
EdU+/pixels
1.5×10-3
1×10-3
5×10-4
0
EGF
siCTRL
siMAP4K4
siSTRN4
siSTRN3
siSTRIP1
MAP4K4+siSTRN3

Figure 4

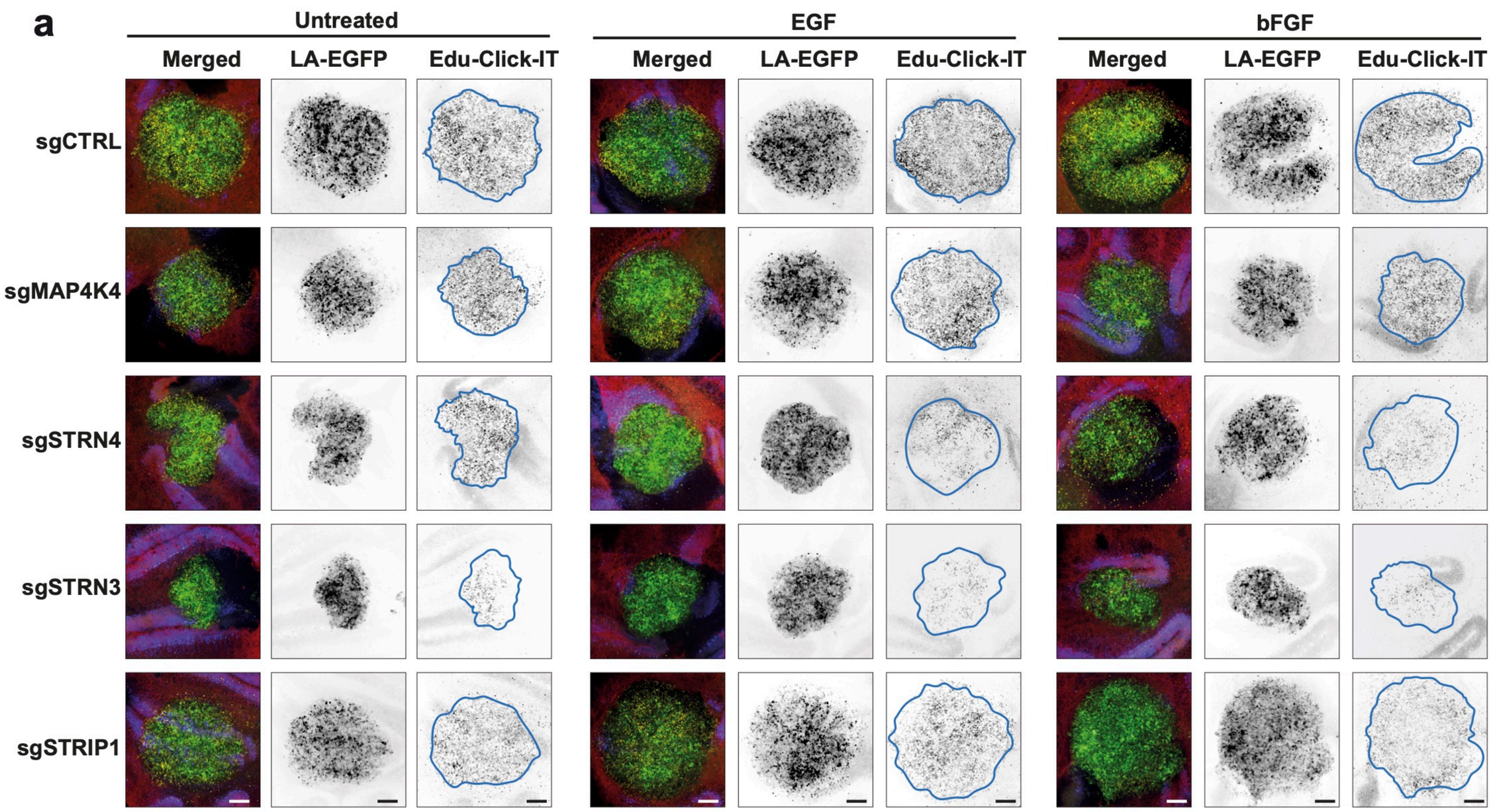
a
Untreated
EGF
bFGF
Merged
LA-EGFP
Edu-Click-IT
sgCTRL
sgMAP4K4
sgSTRN4
sgSTRN3
sgSTRIP1

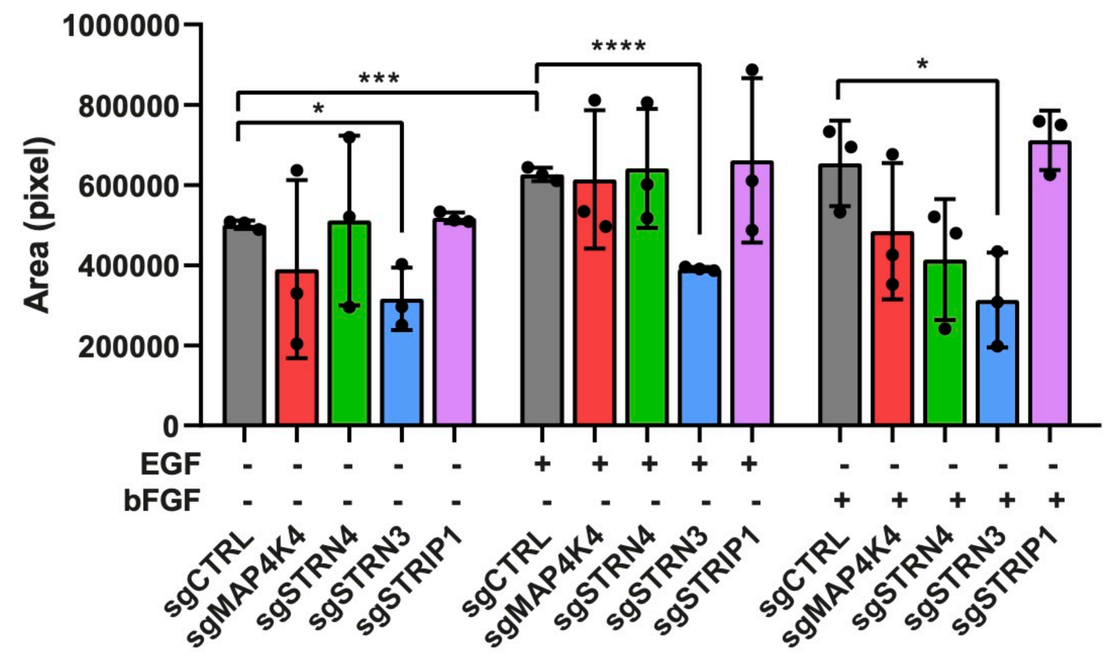
b
Area (pixel)
1000000
800000
600000
400000
200000
0
***
*
****
*
EGF
bFGF
sgCTRL
sgMAP4K4
sgSTRN4
sgSTRN3
sgSTRIP1

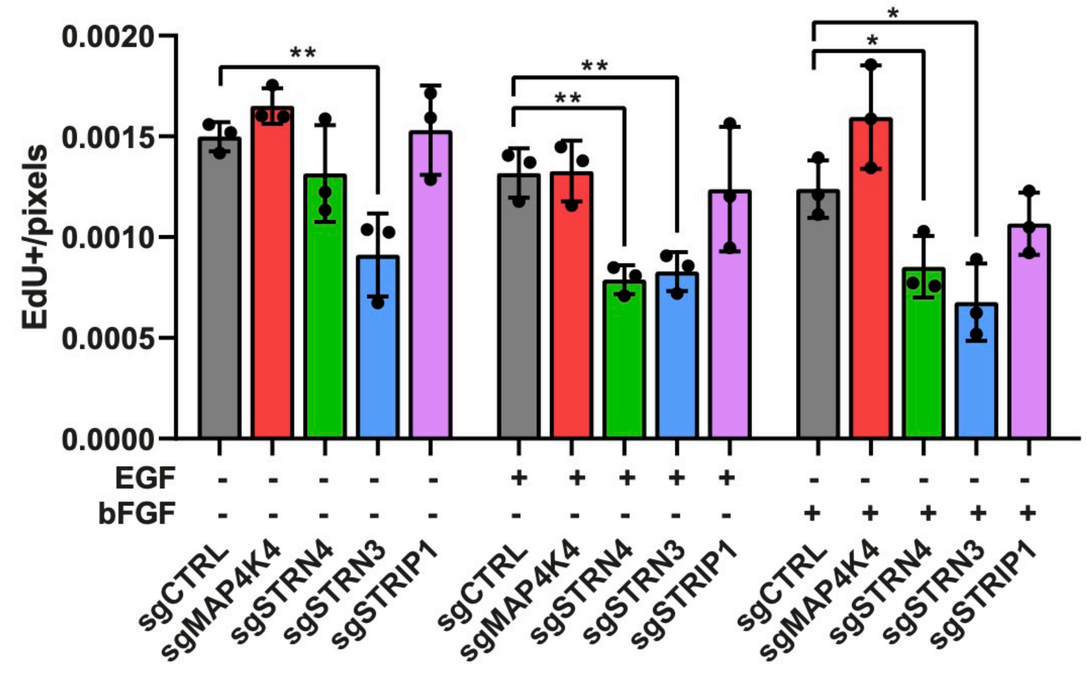
c
EdU+/pixels
0.0020
0.0015
0.0010
0.0005
0.0000
**
**
**
*
*
EGF
bFGF
sgCTRL
sgMAP4K4
sgSTRN4
sgSTRN3
sgSTRIP1

Figure 5

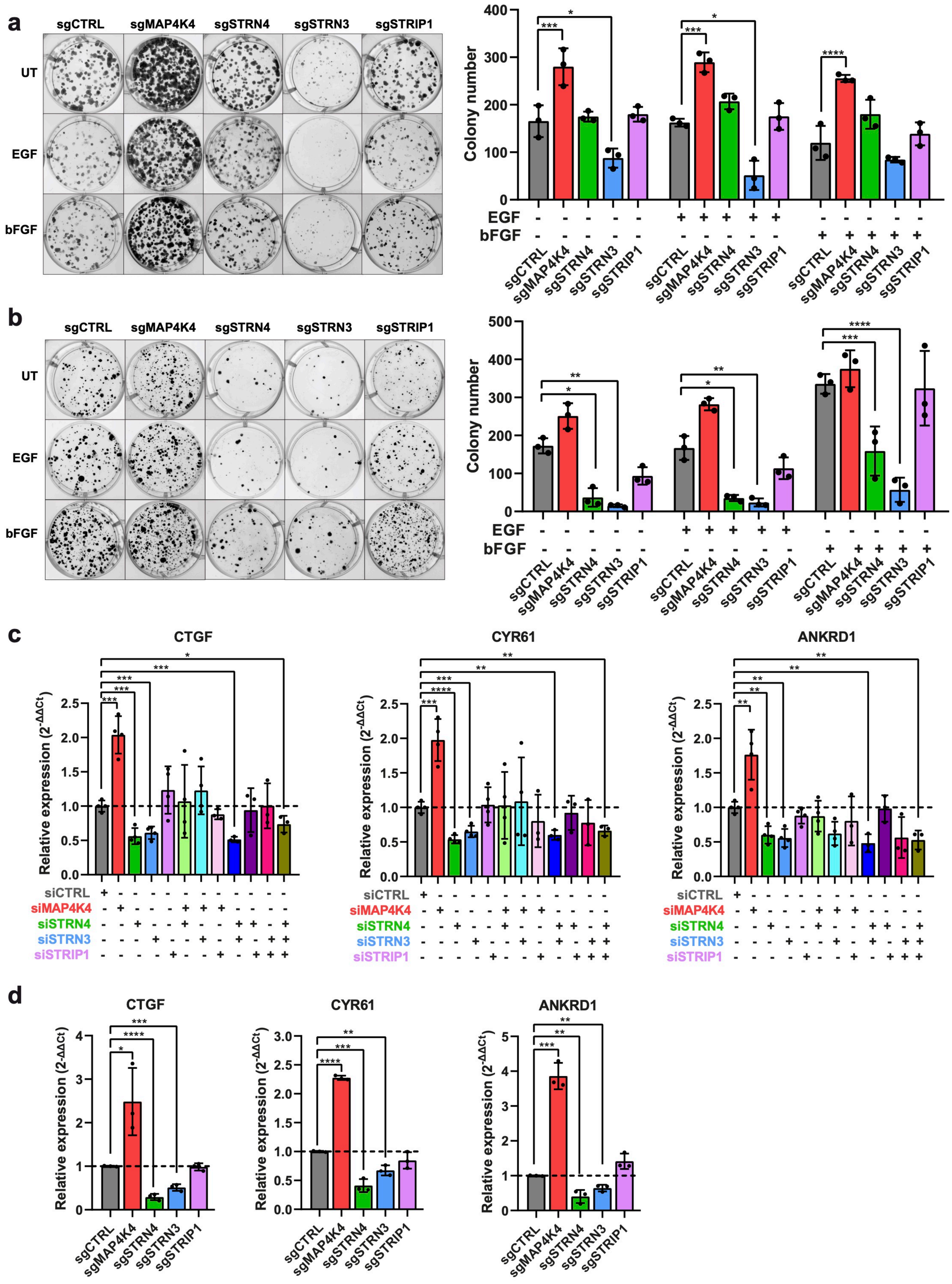
a
sgCTRL
sgMAP4K4
sgSTRN4
sgSTRN3
sgSTRIP1
UT
EGF
bFGF
Colony number
EGF
bFGF
b
c
CTGF
CYR61
ANKRD1
Relative expression ($2^{-\Delta\Delta Ct}$)
siCTRL
siMAP4K4
siSTRN4
siSTRN3
siSTRIP1
d

Figure 6

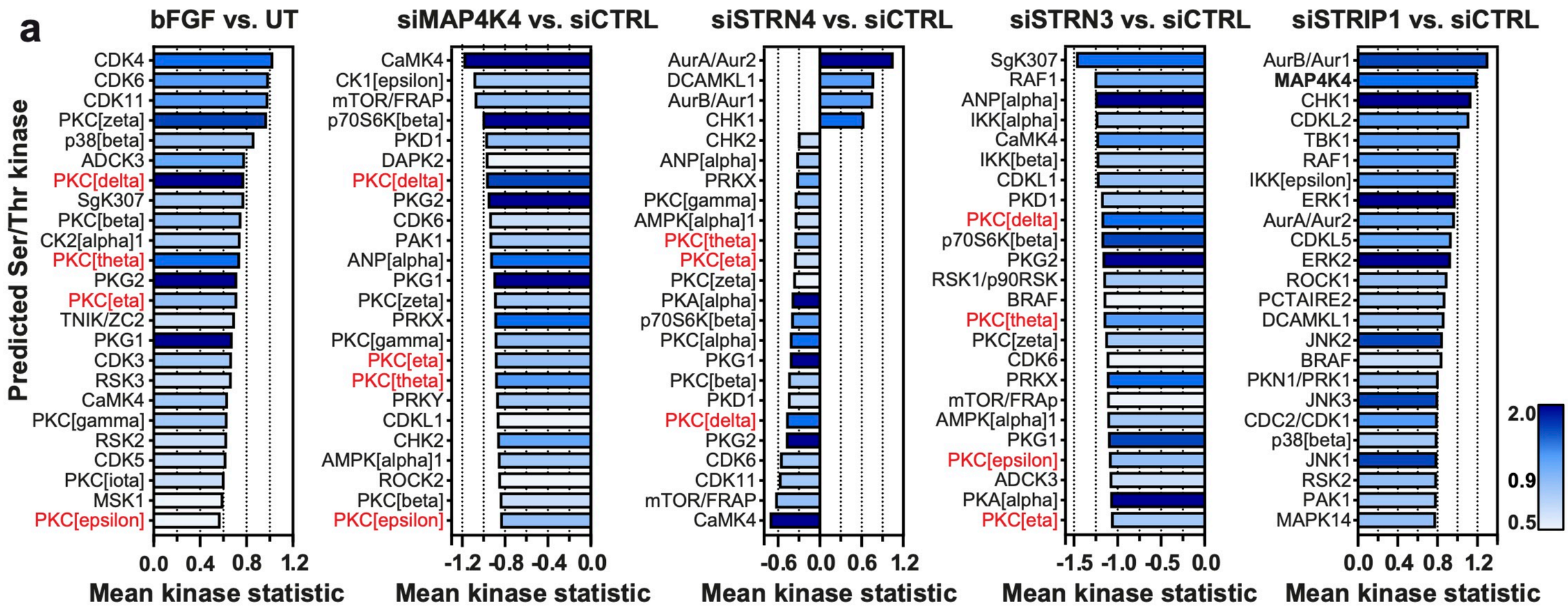
a
bFGF vs. UT
siMAP4K4 vs. siCTRL
siSTRN4 vs. siCTRL
siSTRN3 vs. siCTRL
siSTRIP1 vs. siCTRL
Predicted Ser/Thr kinase
CDK4
CDK6
CDK11
PKC[zeta]
p38[beta]
ADCK3
PKC[delta]
SgK307
PKC[beta]
CK2[alpha]1
PKC[theta]
PKG2
PKC[eta]
TNIK/ZC2
PKG1
CDK3
RSK3
CaMK4
PKC[gamma]
RSK2
CDK5
PKC[iota]
MSK1
PKC[epsilon]
CaMK4
CK1[epsilon]
mTOR/FRAP
p70S6K[beta]
PKD1
DAPK2
PKC[delta]
PKG2
CDK6
PAK1
ANP[alpha]
PKG1
PKC[zeta]
PRKX
PKC[gamma]
PKC[eta]
PKC[theta]
PRKY
CDKL1
CHK2
AMPK[alpha]1
ROCK2
PKC[beta]
PKC[epsilon]
AurA/Aur2
DCAMKL1
AurB/Aur1
CHK1
CHK2
ANP[alpha]
PRKX
PKC[gamma]
AMPK[alpha]1
PKC[theta]
PKC[eta]
PKC[zeta]
PKA[alpha]
p70S6K[beta]
PKC[alpha]
PKG1
PKC[beta]
PKD1
PKC[delta]
PKG2
CDK6
CDK11
mTOR/FRAP
CaMK4
SgK307
RAF1
ANP[alpha]
IKK[alpha]
CaMK4
IKK[beta]
CDKL1
PKD1
PKC[delta]
p70S6K[beta]
PKG2
RSK1/p90RSK
BRAF
PKC[theta]
PKC[zeta]
CDK6
PRKX
mTOR/FRAp
AMPK[alpha]1
PKG1
PKC[epsilon]
ADCK3
PKA[alpha]
PKC[eta]
AurB/Aur1
MAP4K4
CHK1
CDKL2
TBK1
RAF1
IKK[epsilon]
ERK1
AurA/Aur2
CDKL5
ERK2
ROCK1
PCTAIRE2
DCAMKL1
JNK2
BRAF
PKN1/PRK1
JNK3
CDC2/CDK1
p38[beta]
JNK1
RSK2
PAK1
MAPK14
0.0 0.4 0.8 1.2
-1.2 -0.8 -0.4 0.0
-0.6 0.0 0.6 1.2
-1.5 -1.0 -0.5 0.0
0.0 0.4 0.8 1.2
Mean kinase statistic
2.0
0.9
0.5

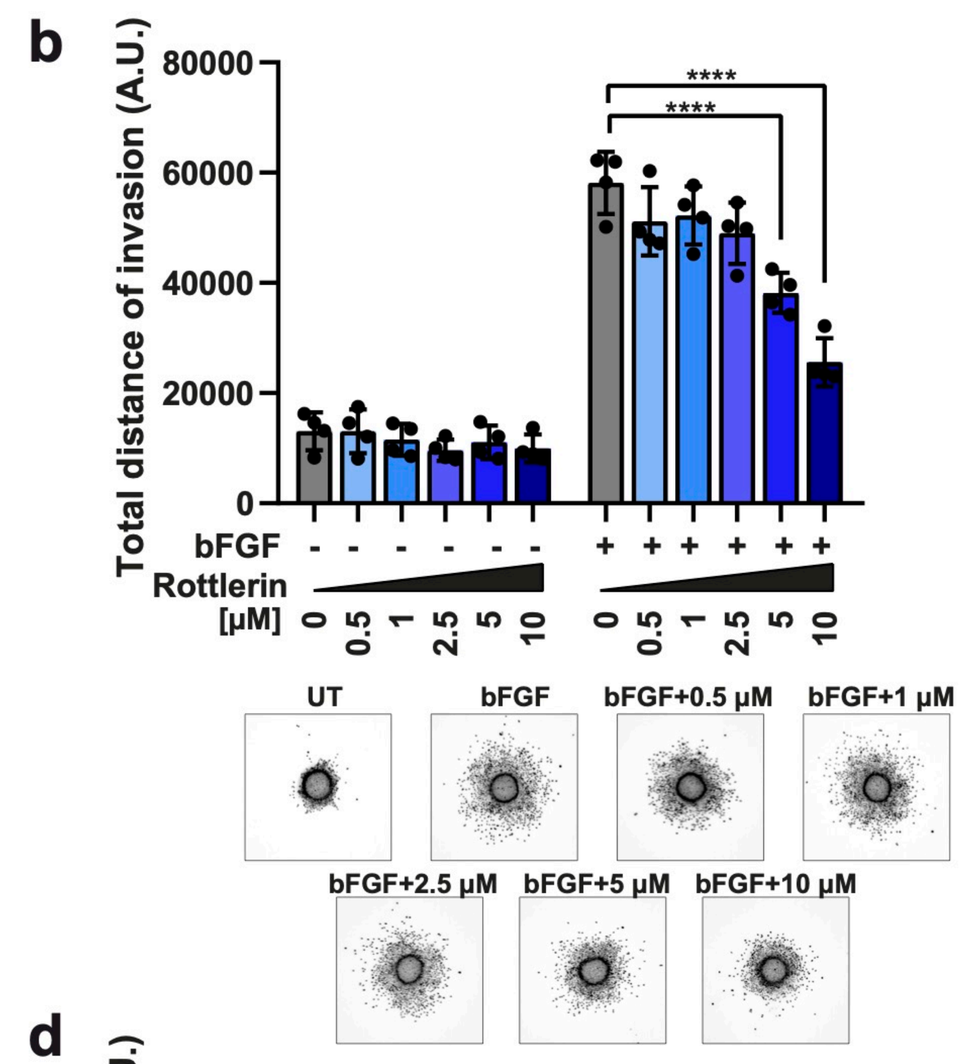
b
Total distance of invasion (A.U.)
80000
60000
40000
20000
0
****
****
bFGF
Rottlerin [μM]
0 0.5 1 2.5 5 10
0 0.5 1 2.5 5 10
UT
bFGF
bFGF+0.5 μM
bFGF+1 μM
bFGF+2.5 μM
bFGF+5 μM
bFGF+10 μM

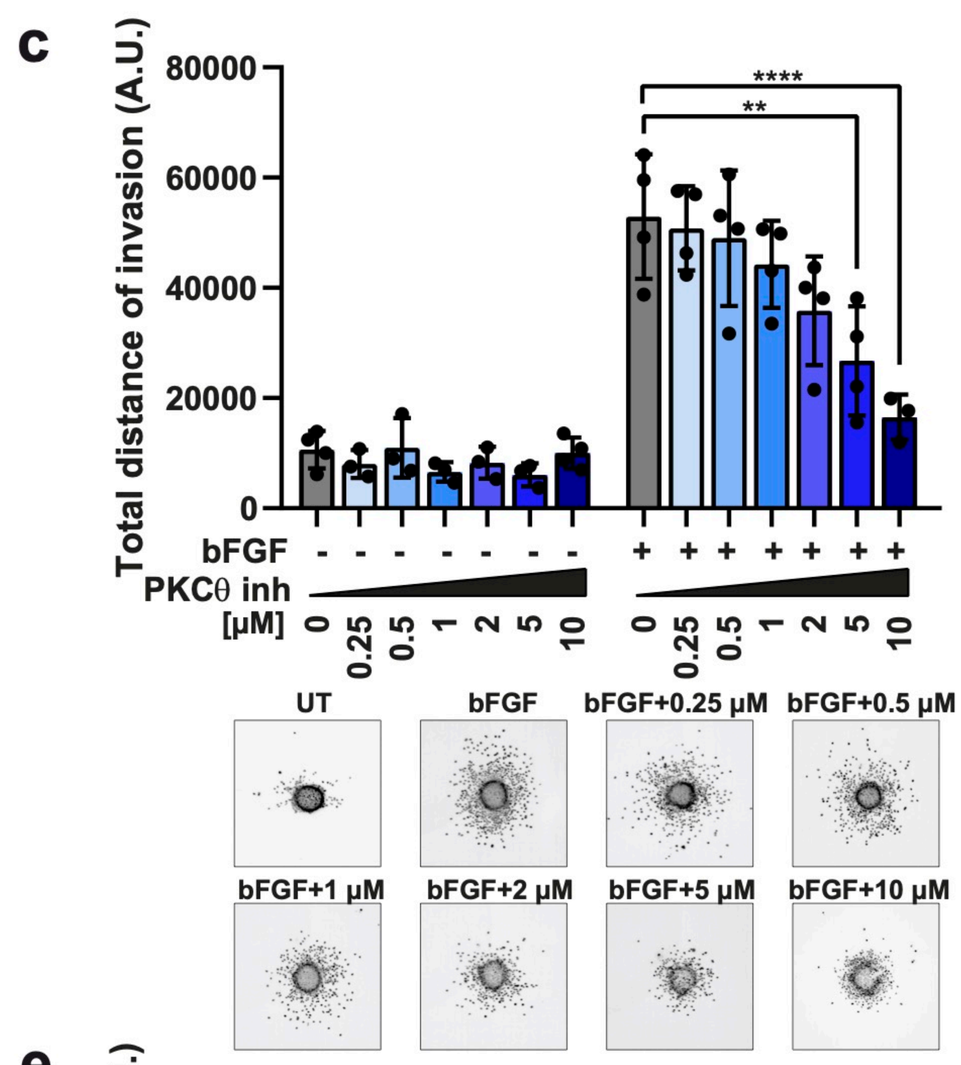
c
Total distance of invasion (A.U.)
80000
60000
40000
20000
0
****
**
bFGF
PKCθ inh [μM]
0 0.25 0.5 1 2 5 10
0 0.25 0.5 1 2 5 10
UT
bFGF
bFGF+0.25 μM
bFGF+0.5 μM
bFGF+1 μM
bFGF+2 μM
bFGF+5 μM
bFGF+10 μM

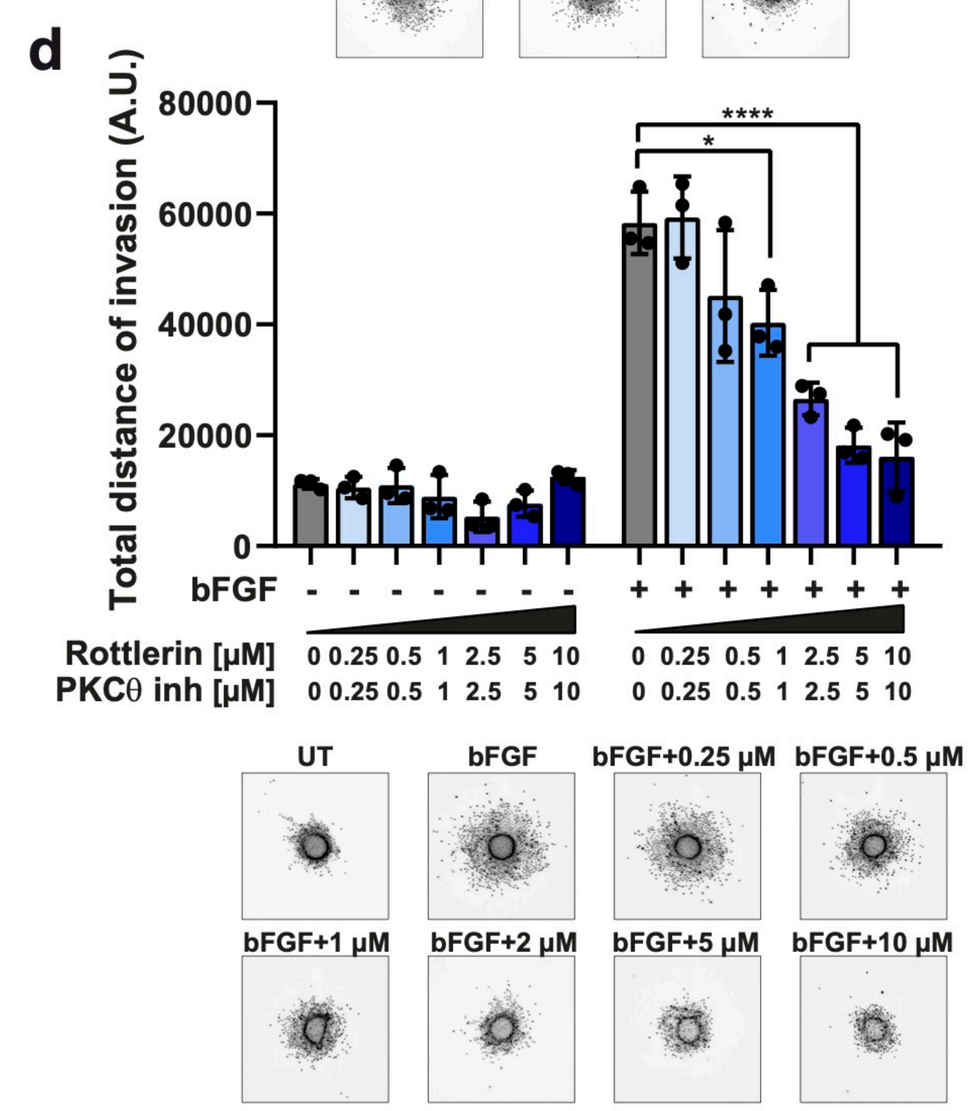
d
Total distance of invasion (A.U.)
80000
60000
40000
20000
0
****
*
bFGF
Rottlerin [μM]
0 0.25 0.5 1 2.5 5 10
0 0.25 0.5 1 2.5 5 10
PKCθ inh [μM]
0 0.25 0.5 1 2.5 5 10
0 0.25 0.5 1 2.5 5 10
UT
bFGF
bFGF+0.25 μM
bFGF+0.5 μM
bFGF+1 μM
bFGF+2 μM
bFGF+5 μM
bFGF+10 μM

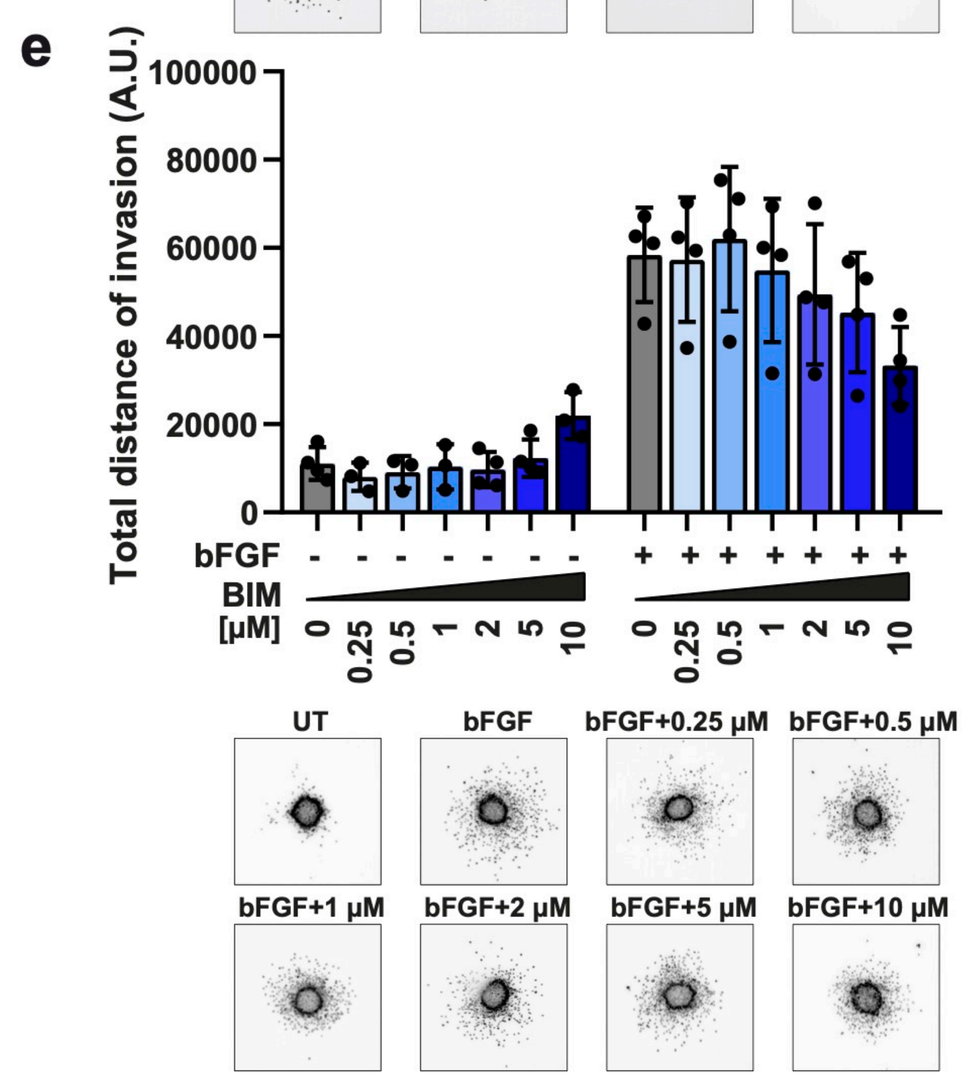
e
Total distance of invasion (A.U.)
100000
80000
60000
40000
20000
0
bFGF
BIM [μM]
0 0.25 0.5 1 2 5 10
0 0.25 0.5 1 2 5 10
UT
bFGF
bFGF+0.25 μM
bFGF+0.5 μM
bFGF+1 μM
bFGF+2 μM
bFGF+5 μM
bFGF+10 μM

Figure 7

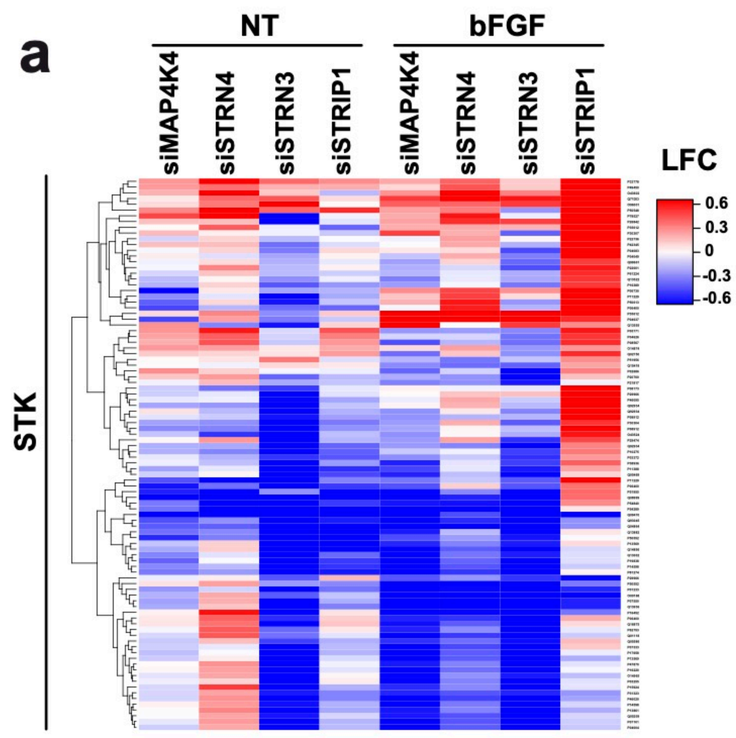
a
NT
bFGF
siMAP4K4
siSTRN4
siSTRN3
siSTRIP1
LFC
STK
0.6
0.3
0
-0.3
-0.6

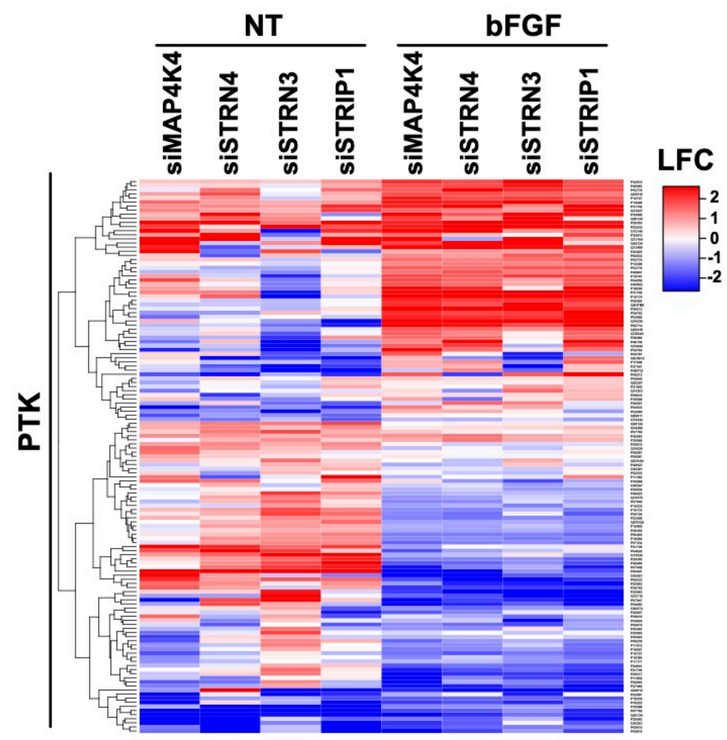
NT
bFGF
siMAP4K4
siSTRN4
siSTRN3
siSTRIP1
LFC
PTK
2
1
0
-1
-2

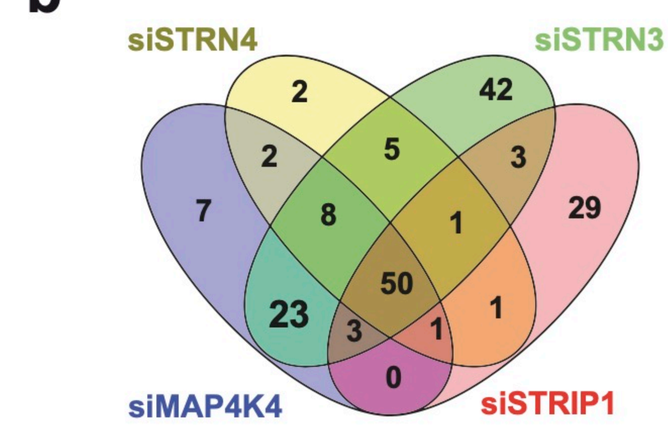
b
siSTRN4
siSTRN3
siMAP4K4
siSTRIP1
2
42
2
5
3
7
8
1
29
50
23
3
1
1
0

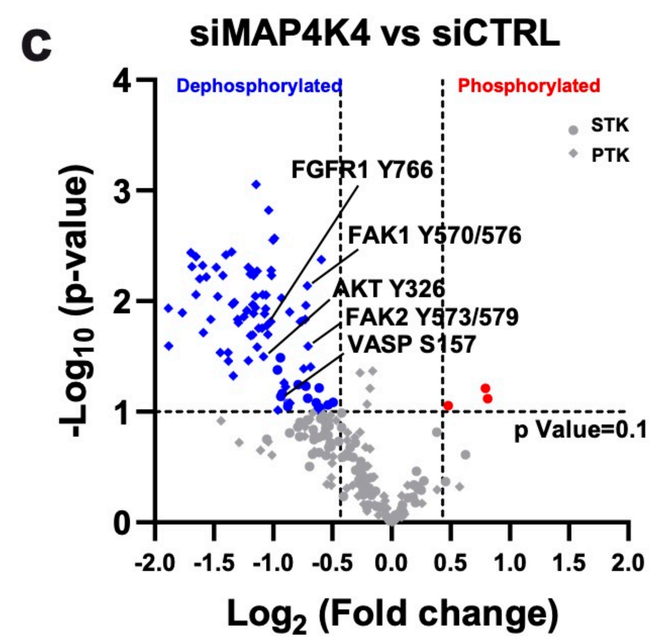
c
siMAP4K4 vs siCTRL
Dephosphorylated
Phosphorylated
STK
PTK
FGFR1 Y766
FAK1 Y570/576
AKT Y326
FAK2 Y573/579
VASP S157
p Value=0.1
-Log10 (p-value)
Log2 (Fold change)

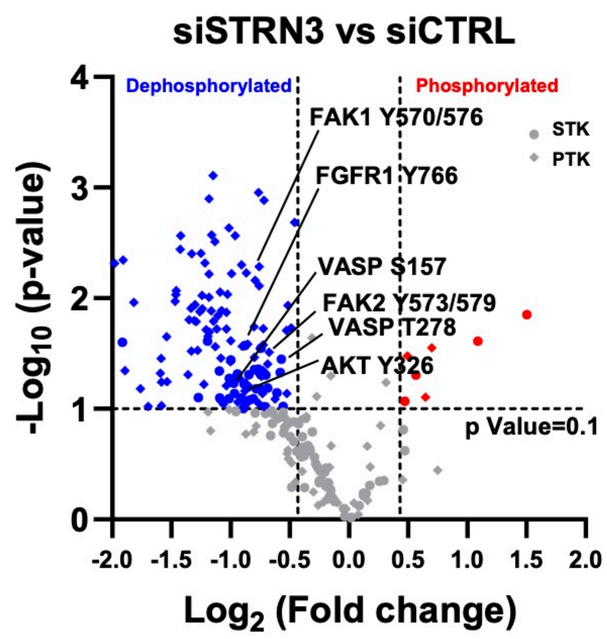
siSTRN3 vs siCTRL
Dephosphorylated
Phosphorylated
FAK1 Y570/576
FGFR1 Y766
STK
PTK
VASP S157
FAK2 Y573/579
VASP T278
AKT Y326
p Value=0.1
-Log10 (p-value)
Log2 (Fold change)

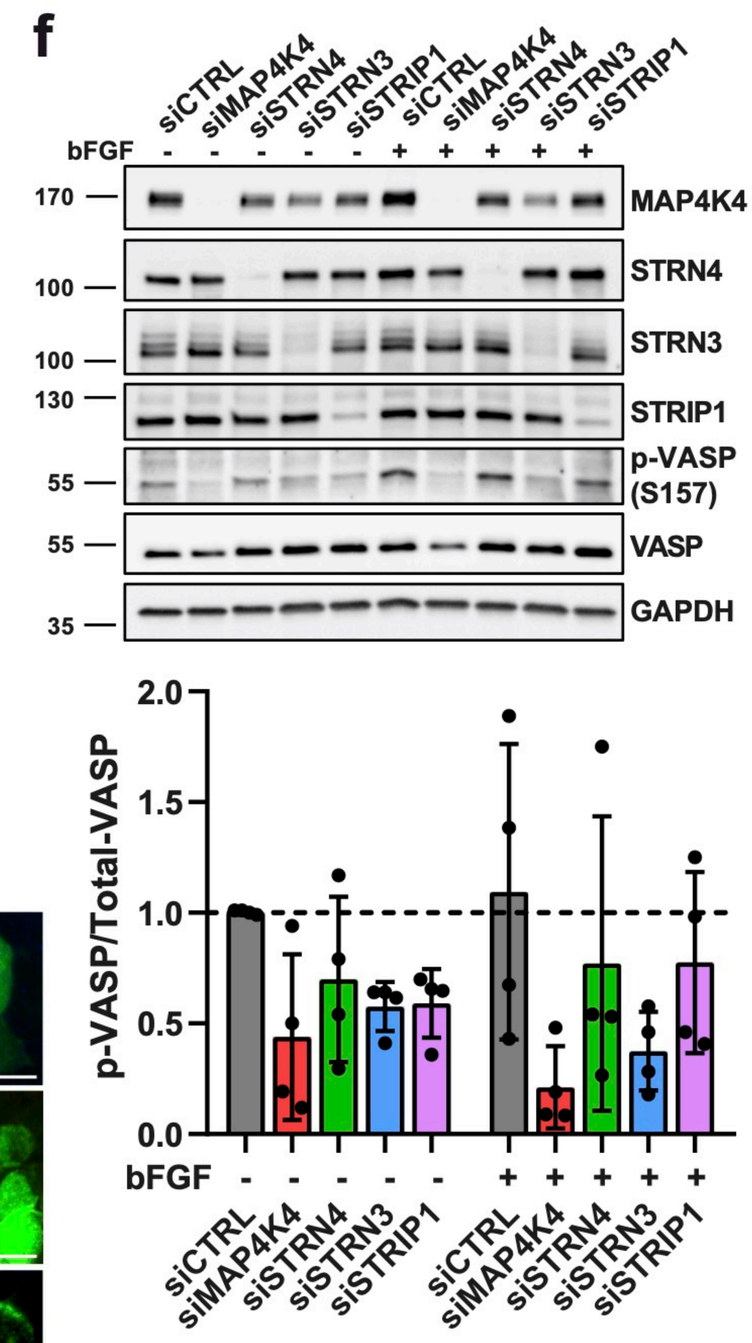
f
siCTRL
siMAP4K4
siSTRN4
siSTRN3
siSTRIP1
bFGF
170
100
100
130
55
55
35
MAP4K4
STRN4
STRN3
STRIP1
p-VASP (S157)
VASP
GAPDH
p-VASP/Total-VASP

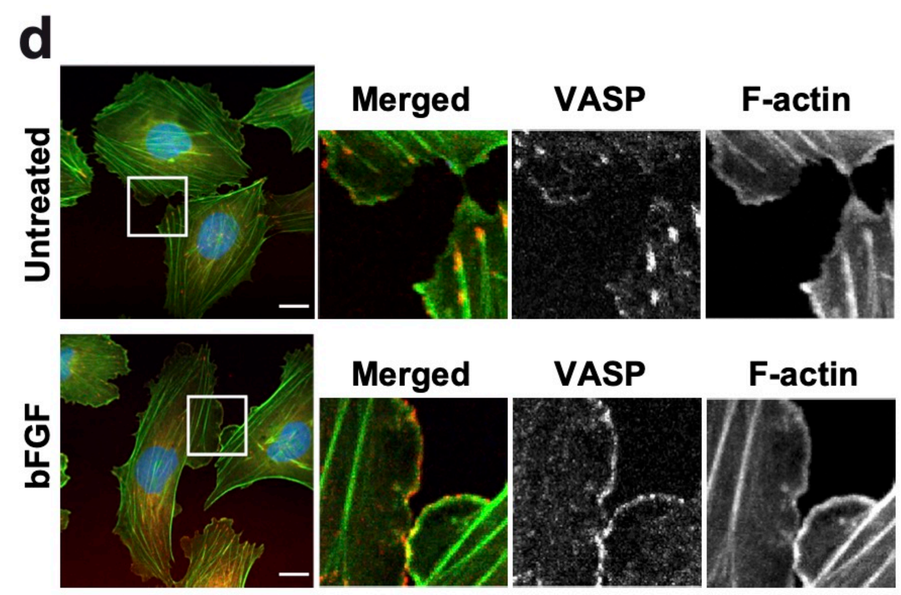
d
Untreated
bFGF
Merged
VASP
F-actin

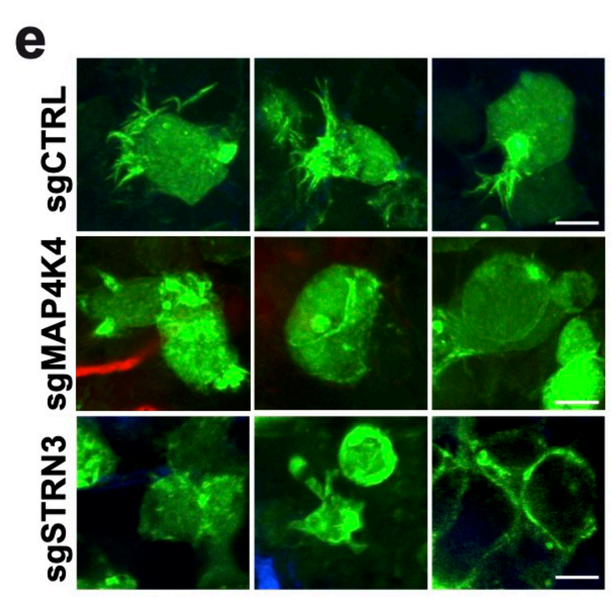
e
sgCTRL
sgMAP4K4
sgSTRN3

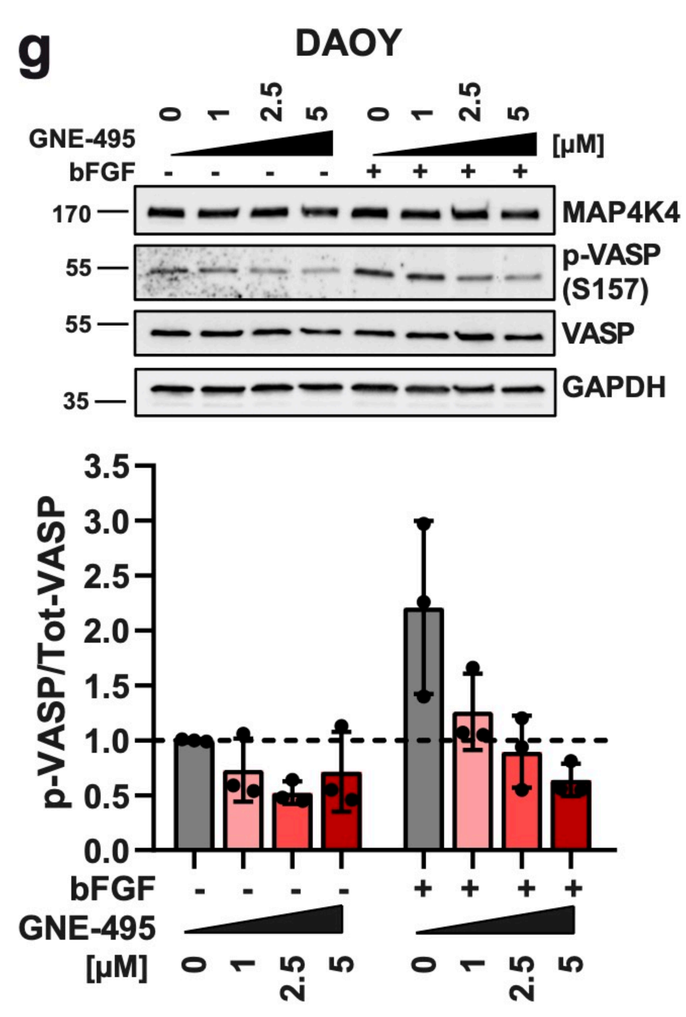
g
DAOY
GNE-495
[μM]
bFGF
170
55
55
35
MAP4K4
p-VASP (S157)
VASP
GAPDH
p-VASP/Tot-VASP

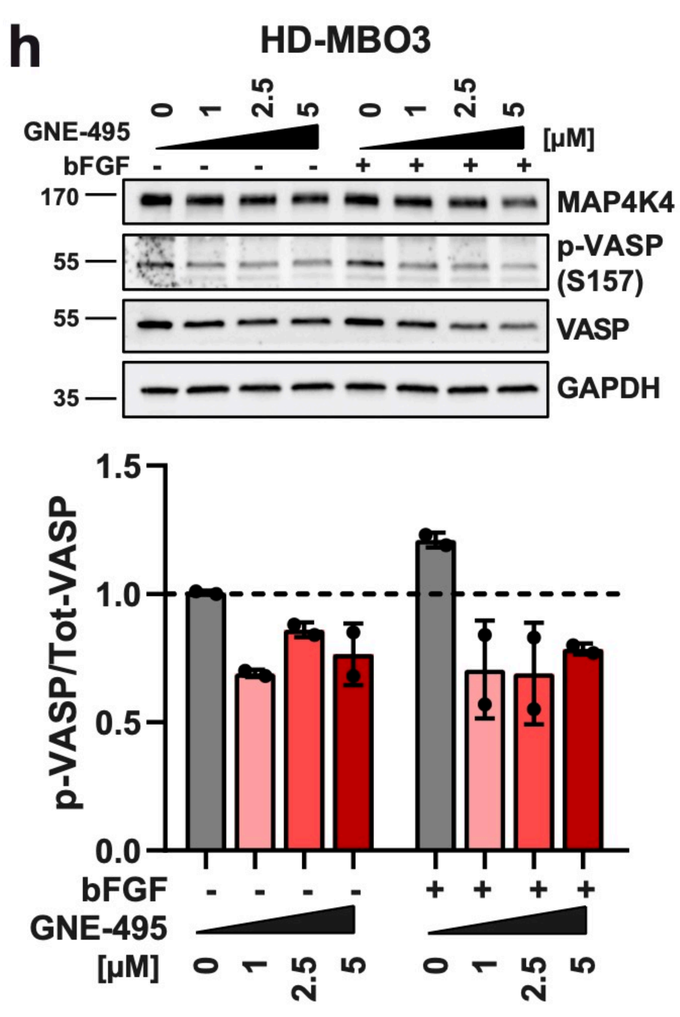
h
HD-MBO3
GNE-495
[μM]
bFGF
170
55
55
35
MAP4K4
p-VASP (S157)
VASP
GAPDH
p-VASP/Tot-VASP

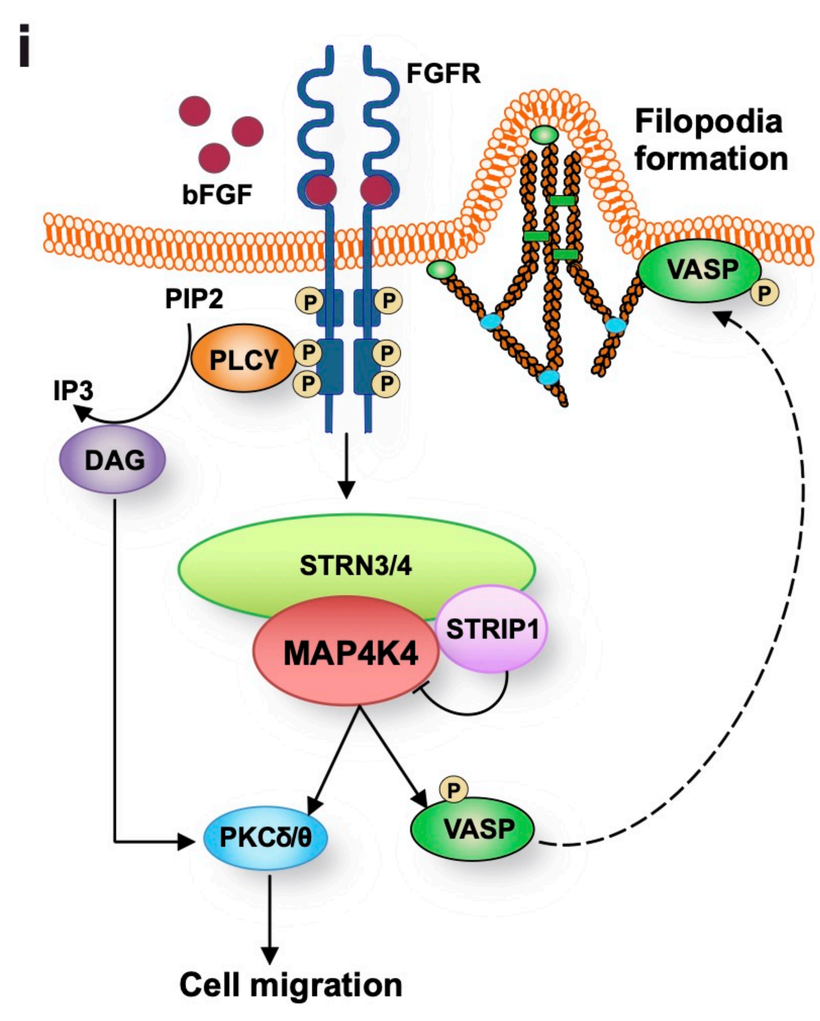
i
FGFR
bFGF
Filopodia formation
VASP
PIP2
PLCγ
IP3
DAG
STRN3/4
MAP4K4
STRIP1
PKCδ/θ
VASP
Cell migration